UNIVERSIDAD DE CANTABRIA

Facultad de Ciencias

Departamento de Física Aplicada

Tesis Doctoral

SYNTHESIS, STRUCTURAL CHARACTERIZATION AND SPECTROSCOPIC STUDY OF NANOCRYSTALLINE AND MICROCRYSTALLINE MATERIALS

Rosa Martín Rodríguez

Santander, Noviembre de 2010

Chapter 5

Insulating materials. Luminescent properties

5.1 Introduction

In this chapter, we present the most relevant results in relation with the electronic transitions responsible for the optical properties of different systems doped with RE and TM ions. The synthesis of these materials has as its main goal the development of new luminescent materials, specially those showing UC emission, and the study of the fundamental physics, in particular the involved UC mechanisms, responsible for this luminescence. First, luminescence properties of Y_2O_3 and $NaYF_4$ nanoparticles doped with Er^{3+} and Yb^{3+} are investigated. The Er^{3+}-Yb^{3+} combination is frequently used in the development of high efficiency UC materials [1], besides, $NaYF_4$ is the most efficient host material up to date for UC phosphors [2]. The underlying mechanisms in UC processes for Tb^{3+}-Yb^{3+} and Eu^{3+}-Yb^{3+} co-doped GGG and YAG nanocrystals are also analyzed. Then, green UC Mn^{2+} luminescence in Mn^{2+}-Yb^{3+} co-doped LMA powders is demonstrated, as far as we know, for the first time up to 650 K. In the last section, the temperature and pressure dependence of the Cr^{3+} transitions in GGG nanoparticles is studied.

5.2 Rare-earth ions doped nanoparticles

UC materials, in which visible light is generated upon IR excitation, have attracted significant attention for advanced applications such as solid state lasers [3], [4], materials

for biological applications like bio-labeling, drug delivery, or diagnostics [5], [6], UC phosphors, IR quantum counter detectors, or efficiency improvement of bifacial solar cells [7]. UC laser systems show several advantages over direct UV excitation; IR excitation reduces the photo-ionization induced degradation of hosts, it does not need high excitation wavelength stability, and the output wavelength is not restricted to a given harmonic [3]. Recently, Prasad *et al.* used upconverting nanophosphors for in vitro and in vivo photoluminescence bio-imaging, providing deeper light penetration into the biological tissues which are transparent in the 750-1000 nm range. The advantage of NIR excitation is the reduction of the background autofluorescence of the tissues [6].

The vast majority of UC studies investigated up to date involve insulating materials doped with RE ions. The energy emission in semiconductors is known to be very sensitive to the system dimensionality and to the particle size [8]. However, due to the localized character of the f electrons, the emission energies associated to f−f transitions in RE ions are mainly independent of the nanocrystals size. On the other hand, the emission intensity and lifetime may change when particle size decreases due to the presence of organic impurities on the nanoparticles surface. The emission intensity can also be modified by the combination of RE ions and by changing the doping concentrations. It is well-known that Yb^{3+} is an excellent UC sensitizer for Er^{3+}, Tm^{3+}, Pr^{3+} or Ho^{3+} ions [1], [9]. All these ions present intermediate states almost resonant with the $^2F_{7/2} \rightarrow {}^2F_{5/2}$ Yb^{3+} transition. The doubly-doped UC systems containing Er^{3+} and Yb^{3+} present the highest UC efficiencies [2]. On the contrary, the situation is completely different for RE ions like Tb^{3+} or Eu^{3+} which have no intermediate levels resonant with Yb^{3+}. Tb^{3+} and Eu^{3+} are attractive as emitting ions because of their high quantum efficiency related to the large energy gap between the emitting states and the low lying ^7F_J ($J=$ 0, 1, …, 7) excited states.

The ability of Yb^{3+} to induce UC is based on the high oscillator strength of the unique f−f transition, $^2F_{7/2} \rightarrow {}^2F_{5/2}$, which is located in the NIR, just in the range of cheap and high power LD. Yb^{3+} has no higher excited states and it is transparent in the visible region. The UC processes involving resonant ions, like in Er^{3+}-Yb^{3+} co-doped materials, can be ascribed to GSA/ESA and/or GSA/ETU mechanisms. Since the Tb^{3+}-Yb^{3+} UC

system was introduced in 1969, many studies have been devoted to these two ions [10], [11], [12], but the fact of getting UC emission in nanoparticles is not so common and always noticeable. However, as far as we know, there are only few examples of UC luminescence in Eu^{3+}-Yb^{3+} systems in the literature [13], [14]. The UC luminescence in Tb^{3+}-Yb^{3+} or Eu^{3+}-Yb^{3+} systems is assigned to a cooperative sensitization mechanism or GSA/ESA processes in dimers.

In this work, nanocrystals of Y_2O_3: Er^{3+}, Yb^{3+}, $NaYF_4$: Er^{3+}, Yb^{3+} as well as Tb^{3+}-Yb^{3+} and Eu^{3+}-Yb^{3+} co-doped GGG and YAG nanoparticles have been prepared by using different synthesis methods. The potential applications of these nanocrystalline materials go through the possibility of reaching the same properties observed in bulk but in systems with dimensions in the range of nanometers. Silica is highly bio-compatible and its surface chemistry is well documented for biological interactions; in this sense, coating with SiO_2 would be the first step in the functionalization of the obtained nanoparticles. XRD, TEM, as well as RT luminescence, excitation and lifetime measurements have been carried out in these samples. The most relevant structural and spectroscopic results in order to characterize them and to identify the UC mechanisms in each case are shown in this section.

5.2.1 Er^{3+}, Yb^{3+} co-doped Y_2O_3

Synthesis and characterization

Within inorganic materials, Y_2O_3 is one of the most widely studied systems for accepting trivalent impurities. It crystallizes in the cubic system, showing a *bixbyte* structure (($Fe,Mn)_2O_3$) with $Ia3$ space group (Fig. 5.1). The unit cell contains 16 molecules and the bulk cell parameter is a_0=10.604 Å [15]. Y^{3+} ions are accommodated in 32 sites in the unit cell; 24 sites with point group symmetry C_2 and 8 sites with C_{3i} symmetry. RE ions substitute Y^{3+} ions and have been found to be randomly distributed in both sites [16]. The C_{3i} site has associated a center of inversion, therefore, f-f electric dipole transitions are much weaker than those related to the C_2 site. The maximum phonon energy in bulk yttria is 600 cm^{-1} [17].

In this work, Y_2O_3: Er^{3+}, Yb^{3+} nanoparticles prepared by two methods, ball milling
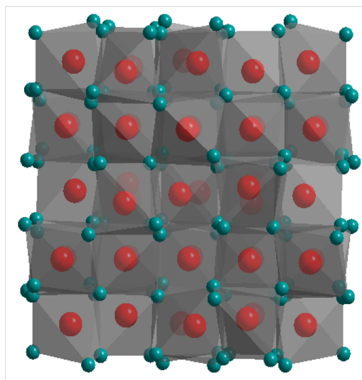
Figure 5.1: Y_2O_3 cubic structure.
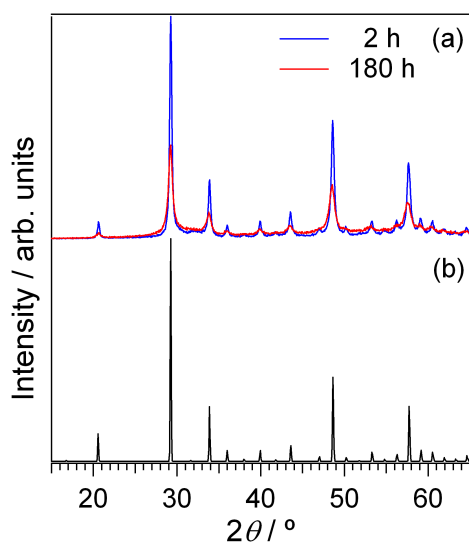
Figure 5.2: XRD patterns of Y_2O_3: 2%Er^{3+}, 1%Yb^{3+} nanoparticles prepared by ball milling for 2 and 180 hours (a), and calculated pattern for cubic Y_2O_3 (a_0=10.604 Å) (b).

(top-down) and combustion (bottom-up) are studied. Both synthesis methods produce nanoparticles of Y_2O_3 cubic phase as it can be seen from XRD pattern. Figure 5.2 shows the XRD patterns of the Y_2O_3: 2%Er^{3+}, 1%Yb^{3+} nanocrystalline samples prepared in the planetary ball mill for 2 and 180 hours milling time according to the parameters defined in Section 3.2. Considering the most intense peak in the XRD diagram for different grinding times (Fig. 5.3), it can be observed that when grinding time increases, the peaks intensity diminishes while their width increases. This broadening is due to both smaller particle size and strains generated during the milling.

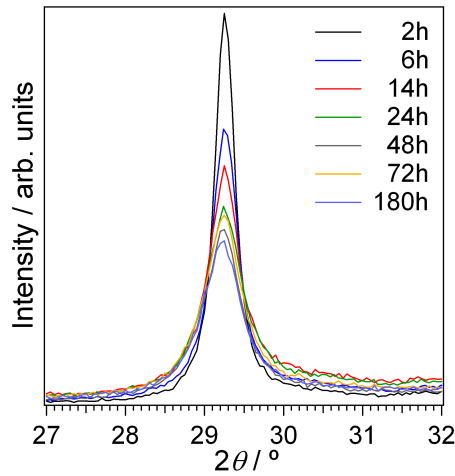According to the Williamson-Hall equation (eq. 4.1), the average crystallite size can

Figure 5.3: Y_2O_3: $2\%Er^{3+}$, $1\%Yb^{3+}$ XRD peak at $2\theta=29.3°$ for different grinding times.
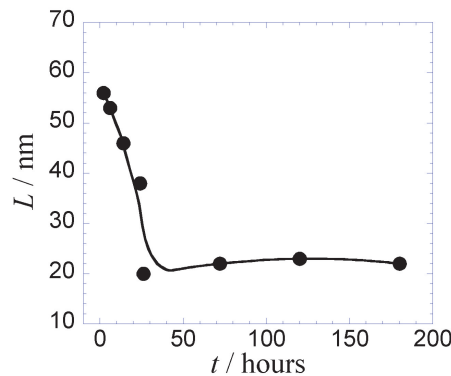

Figure 5.4: Average crystal size, L, for the Y_2O_3: $2\%Er^{3+}$, $1\%Yb^{3+}$ ball milling sample as a function of milling time.

be estimated from XRD diagrams. Considering the dependence of particle size on time (Fig. 5.4), we realize that for times longer than 35 hours a steady-state particle size of 25 nm is reached. This limit value is a characteristic feature of each kind of material and grinding process. We can conclude then, that the optimal milling time for doped Y_2O_3 samples is around 50 hours.

Er^{3+} and Yb^{3+} co-doped Y_2O_3 nanoparticles have also been prepared following the glycine-nitrate solution combustion synthesis (reaction 3.4). Figure 5.5 shows the XRD patterns obtained for a sample prepared by this method before and after it was treated at 500 °C. It can be seen from the peaks broadening that in both cases the particle size is in

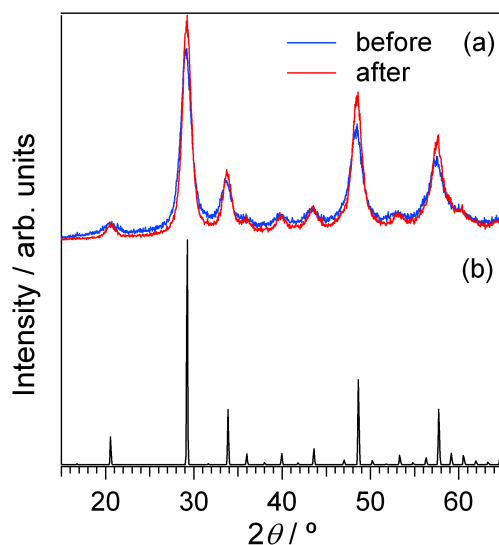Figure 5.5: XRD patterns of Y_2O_3: $2\%Er^{3+}$, $1\%Yb^{3+}$ nanocrystals prepared by combustion before and after firing at 500 °C (a), and calculated pattern for cubic Y_2O_3 ($Ia3$ space group) (b).
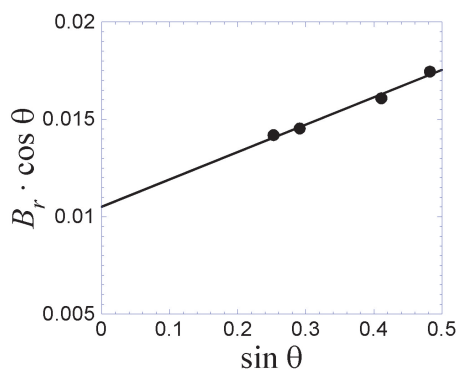

Figure 5.6: Fitting of the experimental peak broadening to the Williamson-Hall equation for Y_2O_3: $2\%Er^{3+}$, $1\%Yb^{3+}$ nanoparticles prepared by combustion and fired at 500 °C for 1 hour.

the nanometer range. The fitting of the experimental peak broadening to the Williamson-Hall equation for Y_2O_3: $2\%Er^{3+}$, $1\%Yb^{3+}$ samples prepared by combustion and calcined (Fig. 5.6) is given by $B_r \cos\theta = 0.01053 + 0.01407 \sin\theta$. The average particle size of the nanoparticles obtained by combustion is about 10 nm before calcination and it increases to 15 nm after firing at 500 °C for 1 hour.

The presence of CO_3^{2-} and OH^- anionic groups on the nanoparticles surface is known to be one of the main reasons for the diminishing of the emission intensity as well as for the reduction of the emission lifetime. These ions contribute with high energy phonons increasing the non-radiative relaxation processes via multiphonon relaxation according to
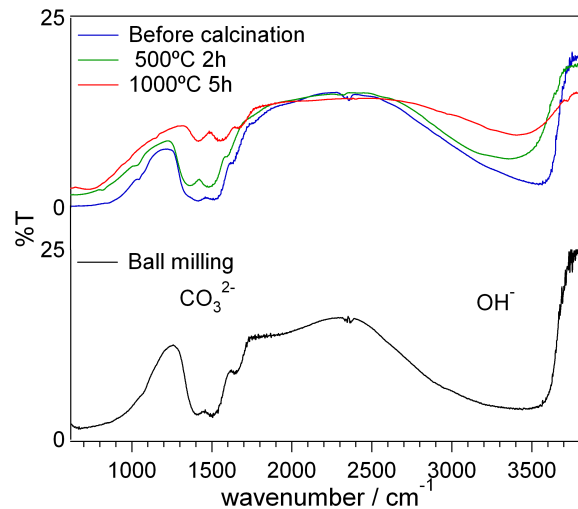
Figure 5.7: IR spectra of nanocrystalline Y_2O_3: $2\%Er^{3+}$, $1\%Yb^{3+}$ prepared by combustion (up) and ball milling (down). Sequential heat treatments have been carried out on combustion samples: 500 °C for 2 hours, and 1000 °C for 5 h.

the gap's law [17]. Moreover, this fact reveals surface effects in the luminescence properties of nanocrystalline materials. The adsorption of these anionic groups is related to the precursors used in the combustion synthesis but this cannot be the only reason, because they also appear in the samples obtained by ball milling, where the starting materials are free of these ions. In order to reduce surface contamination, different thermal treatments have been performed on the nanocrystalline samples.

Figure 5.7 shows the medium infrared (MIR) spectra of Y_2O_3: $2\%Er^{3+}$, $1\%Yb^{3+}$ prepared by both combustion and ball milling. All spectra show bands at approximately 1500 and 3400 cm^{-1} indicating the presence of CO_3^{2-} and OH^- ions on the nanoparticles surface. The intensity of these bands is reduced as calcination time and temperature increase. The best nanoparticles were obtained after calcination at 1000 °C for 5 hours. Nevertheless, several hours after the heat treatment, the nanocrystalline samples were able to adsorb again these anions.

Samples must be fired in order to reduce surface contamination but longer thermal treatments at higher temperature sinterize the powders forming larger nanoparticles. Figure 5.8 presents the particle size dependence on calcination temperature, T_C, and time, t_C, for Y_2O_3: $2\%Er^{3+}$, $1\%Yb^{3+}$ combustion sample. It is observed that nanocrystals size increases for longer firing times and higher temperatures.

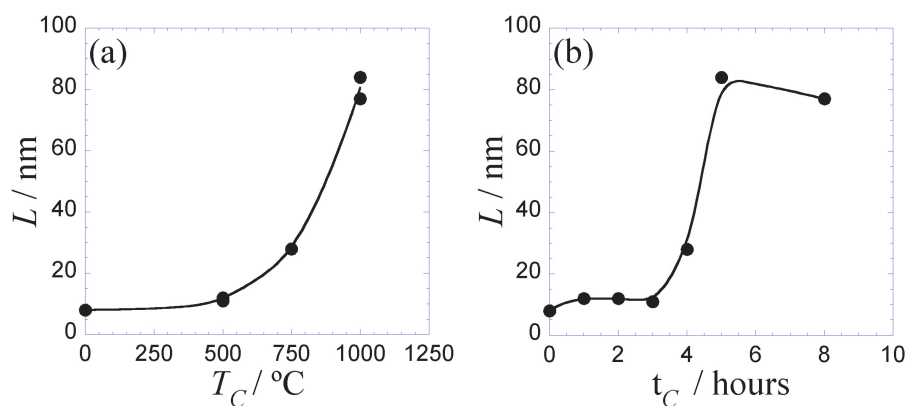Figure 5.8: Variation of Y_2O_3: $2\%Er^{3+}$, $1\%Yb^{3+}$ nanoparticles size, L, as a function of the calcination temperature (a), and time (b).

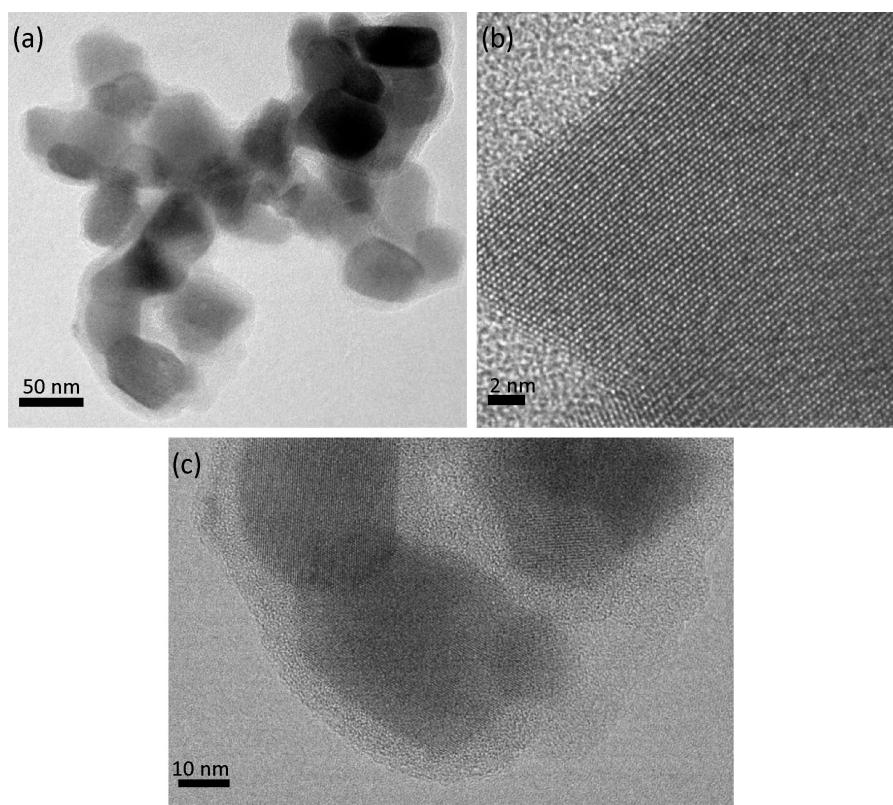Figure 5.9: TEM image of Y_2O_3: $2\%Er^{3+}$, $1\%Yb^{3+}$ prepared by combustion after SiO_2 coating. In the HRTEM images (b) and (c), the observed interplanar distances (0.33 nm) corresponds to the (222) crystal plane.

Bearing in mind both effects, surface contamination and particle size, all Y_2O_3 samples studied in this work were fired at 900 °C for an hour, and closed in shielded capillaries. This covering was performed in order to avoid further contamination which produces a deterioration of their optical properties. Some of the samples were also SiO_2 coated. A final average diameter of 50 nm has been estimated from the peak width of the XRD (see Fig. 5.8). This value is in very good agreement with TEM results shown in figure 5.9. TEM images of coated Y_2O_3 nanoparticles show a SiO_2 shell thickness of about 5-10 nm.

Optical properties

Optical properties of Y_2O_3: 2%Er^{3+}, 1%Yb^{3+} and Y_2O_3: 2%Er^{3+}, 20%Yb^{3+} nanoparticles prepared by high energy ball milling and combustion synthesis are analyzed.

- **Synthesis method and concentration dependence.**

  Figure 5.10 shows the RT diffuse reflectance spectrum of Y_2O_3: 2%Er^{3+}, 20%Yb^{3+} prepared by ball milling. The absorption peaks correspond to Er^{3+} transitions from the ground state, $^4I_{15/2}$, to different excited states, and to the $^2F_{7/2} \rightarrow {}^2F_{5/2}$ Yb^{3+} transition.
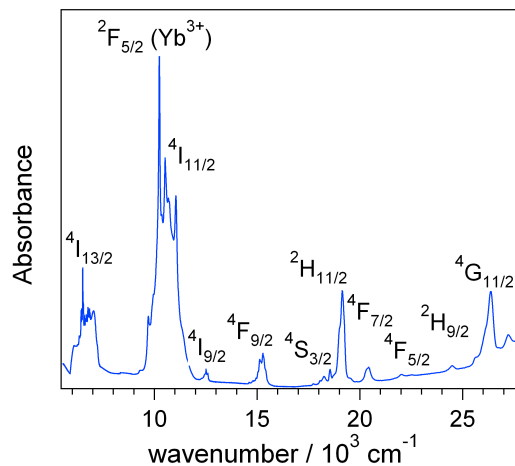

Figure 5.10: RT diffuse reflectance spectrum of Y_2O_3: 2%Er^{3+}, 20%Yb^{3+} prepared by ball milling.

  Figures 5.11 and 5.12 compare the RT luminescence spectra of Y_2O_3 doped with different Er^{3+} and Yb^{3+} concentrations, and prepared by ball milling and combustion, upon direct Er^{3+} excitation at 26596 cm^{-1}, and IR excitation at 10256 cm^{-1}.

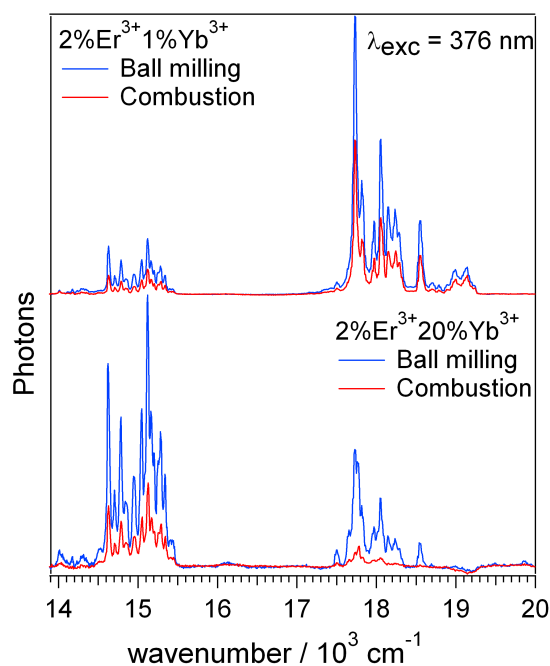Figure 5.11: RT emission of nanocrystalline Y_2O_3 co-doped with different concentrations of Er^{3+} and Yb^{3+} upon excitation at 26596 cm^{-1}. Measurements were performed under the same experimental conditions.
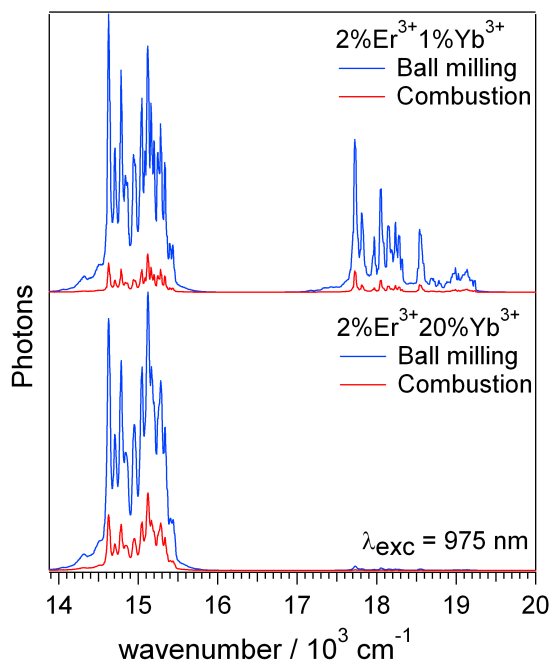

Figure 5.12: RT UC luminescence of Y_2O_3: Er^{3+}, Yb^{3+} nanoparticles with different RE concentrations upon excitation at 10256 cm^{-1}. Measurements were performed under the same experimental conditions.
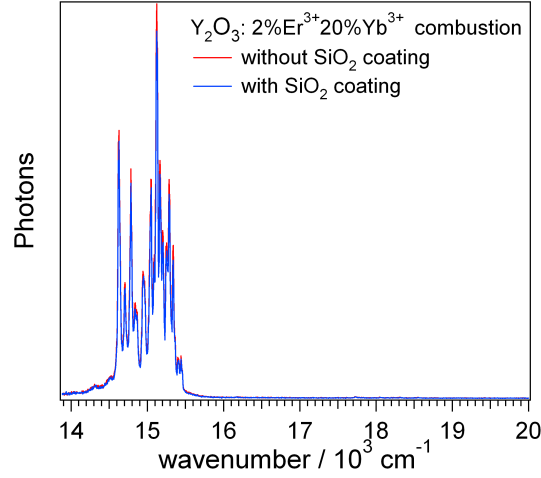
Figure 5.13: RT UC luminescence of Y_2O_3: $2\%Er^{3+}$, $20\%Yb^{3+}$ nanoparticles prepared by combustion, upon excitation at 10256 cm^{-1}, with and without SiO_2 coating.

Emission peaks around 15000 and 18000 cm^{-1} are assigned, respectively, to the transitions from the $^4F_{9/2}$ and the thermalized $(^2H_{11/2}, \,^4S_{3/2})$ excited states, to the $^4I_{15/2}$ ground state of Er^{3+} ions (Fig. 5.14). Figure 5.13 shows the UC emission spectra of Y_2O_3: $2\%Er^{3+}$, $20\%Yb^{3+}$ nanoparticles prepared by combustion with and without SiO_2. The total intensity as well as the intensity ratio between red and green emissions in the spectra of the nanoparticles with and without SiO_2 coating are exactly the same.

From the spectra in Fig. 5.11, we conclude that samples prepared by ball milling have higher luminescence intensities than combustion samples. This is due to the presence of CO_3^{2-} and OH^- groups which is more important in combustion samples, even after thermal treatment. A salient feature is that in the $2\%Er^{3+}$, $1\%Yb^{3+}$ samples, the intensity of the green emission is higher than the red one. On the contrary, those samples doped with $20\%Yb^{3+}$ have a higher red to green intensity ratio. This reduction in the green luminescence is related to the $(^2H_{11/2}, \,^4S_{3/2})$ + $^2F_{7/2} \rightarrow \,^4I_{11/2} + \,^2F_{5/2}$ CR process between Er^{3+} and Yb^{3+} ions, whose probability increases with increasing Yb^{3+} concentration, and is responsible for the additional $(^2H_{11/2}, \,^4S_{3/2})$ depopulation channel (Fig. 5.14).

Figure 5.12 shows the UC luminescence spectra obtained at RT for Y_2O_3: $2\%Er^{3+}$,
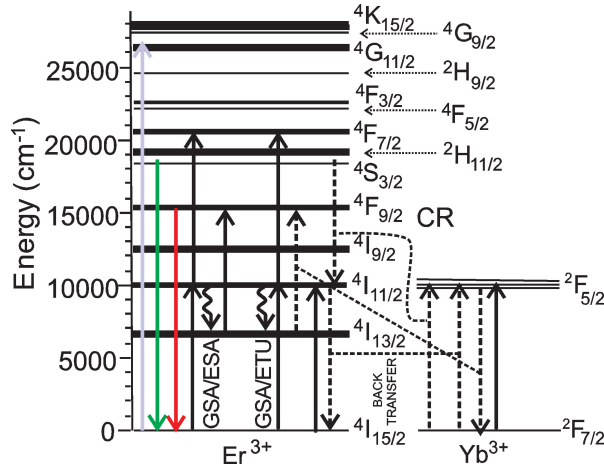
Figure 5.14: Energy level scheme of Er^{3+} and Yb^{3+} ions and the proposed UC mechanisms. Green and red luminescence in Y_2O_3: Er^{3+}, Yb^{3+} samples are depicted. Cross relaxation is responsible for the reduction of green emission. GSA/ESA or GSA/ETU from $^4I_{13/2}$ are responsible for the enhanced red emission upon IR excitation.

1%Yb^{3+} and Y_2O_3: 2%Er^{3+}, 20%Yb^{3+} prepared by mechano-chemical and combustion synthesis upon IR LD excitation centered at 10256 cm^{-1}. The broad excitation ($\Delta\lambda \sim 10$ nm) is able to excite both $^2F_{7/2} \rightarrow {}^2F_{5/2}$ Yb^{3+} and $^4I_{15/2} \rightarrow {}^4I_{11/2}$ Er^{3+} transitions. The same bands around 15000 and 18000 cm^{-1} are observed, and ball milling nanocrystals are once again more efficient than combustion ones. The red UC emission, $^4F_{9/2} \rightarrow {}^4I_{15/2}$, is more intense than the green UC luminescence, $(^2H_{11/2}, {}^4S_{3/2}) \rightarrow {}^4I_{15/2}$ in all cases. For 20%Yb^{3+}-doped nanoparticles the green emission is not detected by the naked eye. The enhancement of red to green emission upon IR excitation can be explained with the following process: after IR excitation, both $^2F_{5/2}$ Yb^{3+} and $^4I_{11/2}$ Er^{3+} multiplets are populated. Yb^{3+} excitation is transferred to the $^4I_{11/2}$ Er^{3+} level by energy transfer (GSA/ETU). Then, most of the ions decay non-radiatively to the $^4I_{13/2}$ level, and Er^{3+} ions can reach the $^4F_{9/2}$ state after the absorption of a second IR photon, ESA, or after another ETU process (Fig. 5.14). In the absence of the $^4I_{11/2} \rightarrow {}^4I_{13/2}$ non-radiative process, a second photon could reach the $(^2H_{11/2}, {}^4S_{3/2})$ green emitting states. This additional mechanism which seems to be more efficient than the $(^2H_{11/2}, {}^4S_{3/2}) \rightarrow {}^4F_{9/2}$ decay, does not exist upon visible excitation.

- **Temporal evolution and UC mechanism.**

Temporal evolution of the red, $^4F_{9/2} \rightarrow {}^4I_{15/2}$, and green, $(^2H_{11/2}, {}^4S_{3/2}) \rightarrow {}^4I_{15/2}$, Er^{3+} luminescence after pulsed excitation with the OPO at 20492 cm^{-1} and 10256 cm^{-1} has been recorded.

Figure 5.15 shows the time dependence of the red and green Er^{3+} luminescence of Y_2O_3: 2%Er^{3+}, 20%Yb^{3+} prepared in the planetary ball mill upon excitation at 20492 cm^{-1}. Experimental data obtained after visible excitation have been fitted to a single exponential, $I(t) = I_0 \exp(\frac{-t}{\tau})$ for all samples. The best fit parameters are shown in Table 5.1. Both emitting states, $^4S_{3/2}$ and $^4F_{9/2}$, show longer lifetimes in ball milling samples in comparison with combustion ones. This fact reveals that the intensity diminishing observed for samples prepared by combustion is related to non-radiative processes, which are more important in samples prepared following the combustion reaction.
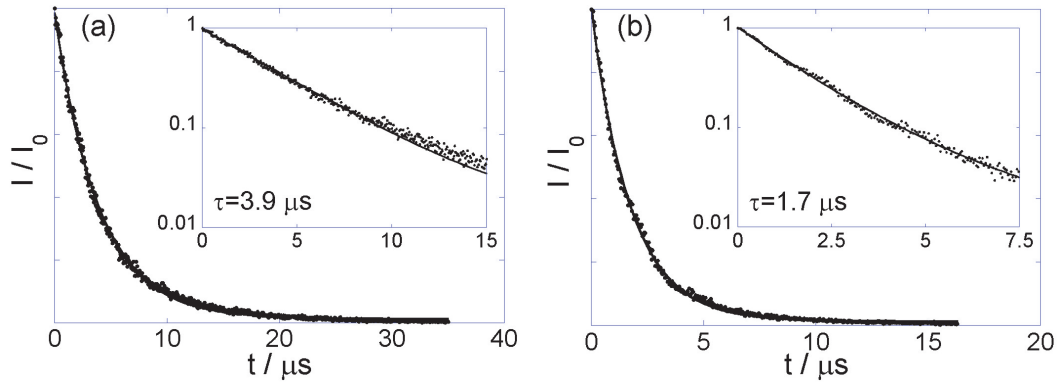

Figure 5.15: Temporal evolution of the RT red (a) and green (b) Er^{3+} luminescence of Y_2O_3: 2%Er^{3+}, 20%Yb^{3+} prepared by ball milling upon excitation at 20492 cm^{-1}.

Figure 5.16 compares the temporal behavior of the red Er^{3+} UC luminescence after IR excitation at 10256 cm^{-1} for Y_2O_3: 2%Er^{3+}, 20%Yb^{3+} prepared by ball milling and combustion synthesis. A rise of the emission intensity followed by a decay is detected in both cases. In this case, the temporal evolution of the Er^{3+} UC emission has been fitted to a Vial's type equation, $I(t) = A \exp(\frac{-t}{B}) - C \exp(\frac{-t}{D})$ [18]. B and D represent the decay and rise of the transient, respectively; hence, B is essentially the inverse of $^4S_{3/2}$ or $^4F_{9/2}$ states lifetime, and D is related to the ETU rate (W_{ETU}) and

Table 5.1: Lifetimes of the $^4F_{9/2}$ and $^4S_{3/2}$ Er^{3+} levels in different Y$_2$O$_3$: Er^{3+}, Yb^{3+} samples detecting at 15129 cm^{-1} and 17730 cm^{-1}, respectively, after direct excitation in the $^4F_{7/2}$ level at 20492 cm^{-1}.

Y$_2$O$_3$: Er^{3+}, Yb^{3+} Sample	$\tau(^4F_{9/2})/\mu$s	$\tau(^4S_{3/2})/\mu$s
2%Er^{3+}, 20%Yb^{3+} Ball milling	3.9 ± 0.2	1.7 ± 0.1
2%Er^{3+}, 20%Yb^{3+} Combustion	2.2 ± 0.1	1.1 ± 0.1
2%Er^{3+}, 1%Yb^{3+} Ball milling	17.6 ± 0.4	4.1 ± 0.2
2%Er^{3+}, 1%Yb^{3+} Combustion	15.3 ± 0.6	2.8 ± 0.2
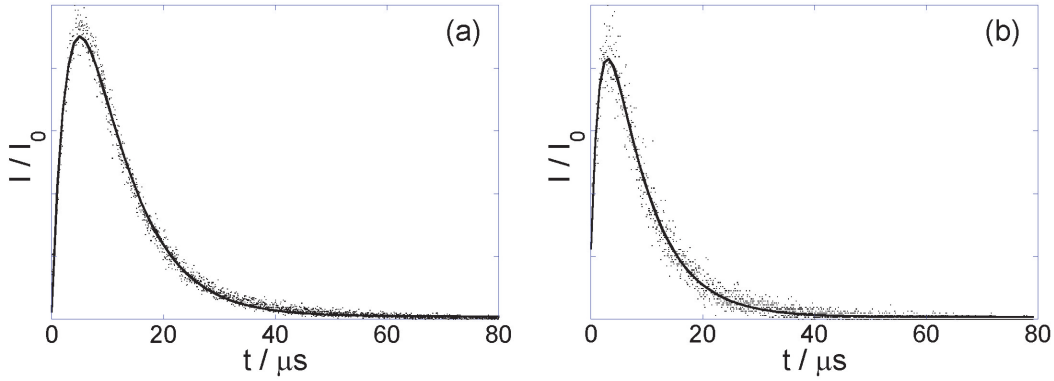
Figure 5.16: Temporal evolution of the RT $^4F_{9/2}$ Er^{3+} UC luminescence of Y$_2$O$_3$: 2%Er^{3+}, 20%Yb^{3+} prepared by ball milling (a) and combustion (b) upon excitation at 10256 cm^{-1}.

$^2F_{5/2}$, $^4I_{11/2}$ lifetimes, according to $D = \frac{1}{\tau(^2F_{5/2})} + \frac{1}{\tau(^4I_{11/2})} + W_{\text{ETU}}$. The best fits for red and green Er^{3+} UC luminescence are shown on Tables 5.2 and 5.3, respectively.

The rise of the luminescence intensity after IR excitation is observed in both red and green UC emissions in all samples. This is a clear proof of an energy transfer process and evidences the contribution of GSA/ETU mechanism to the total UC luminescence. In some cases the rise is not starting from zero, this implies that there is also a contribution of the Er^{3+} single ion GSA/ESA mechanism; that is, after IR excitation, an excited Er^{3+} in the $^4I_{11/2}$ or $^4I_{13/2}$ level can absorb a second photon and be promoted to the $^4F_{9/2}$ or ($^2H_{11/2}$, $^4S_{3/2}$) levels, respectively. Figure 5.17 shows the temporal evolution of the green Er^{3+} UC luminescence of Y$_2$O$_3$: 2%Er^{3+}, 1%Yb^{3+} prepared by ball milling upon excitation at 10256 cm^{-1}. Taking into account that the lifetime of the $^4S_{3/2}$ state in the GSA/ESA process should be exactly the same that after direct Er^{3+} excitation at 20492 cm^{-1}, it is possible to estimate

Table 5.2: Lifetimes of the $^4F_{9/2}$ Er^{3+} level in different Y_2O_3: Er^{3+}, Yb^{3+} samples measured detecting at 15129 cm^{-1} after IR excitation at 10256 cm^{-1} using a Vial's type model (see text).

Y_2O_3: Er^{3+}, Yb^{3+} Sample	B($^4F_{9/2}$)/μs	D($^4F_{9/2}$)/μs
2%Er^{3+}, 20%Yb^{3+} Ball milling	8.4 ± 0.3	3.2 ± 0.2
2%Er^{3+}, 20%Yb^{3+} Combustion	7.5 ± 0.4	1.7 ± 0.2
2%Er^{3+}, 1%Yb^{3+} Ball milling	163 ± 5	1.7 ± 0.1
2%Er^{3+}, 1%Yb^{3+} Combustion	101 ± 7	1.7 ± 0.2

Table 5.3: Lifetimes of the $^4S_{3/2}$ Er^{3+} level in different Y_2O_3: Er^{3+}, Yb^{3+} samples measured detecting at 17730 cm^{-1} after IR excitation at 10256 cm^{-1} using a Vial's type model (see text).

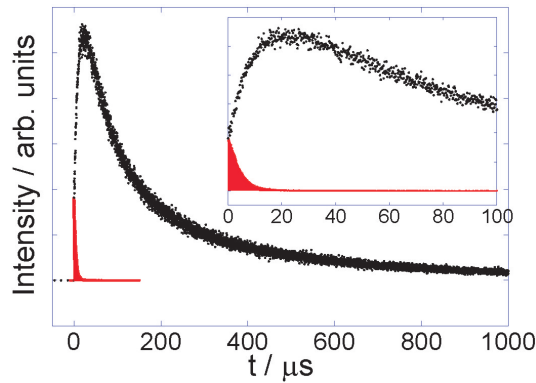| Y_2O_3: Er^{3+}, Yb^{3+} Sample	B($^4S_{3/2}$)/μs	D($^4S_{3/2}$)/μs
2%Er^{3+}, 20%Yb^{3+} Ball milling	3.0 ± 0.1	0.50 ± 0.02
2%Er^{3+}, 20%Yb^{3+} Combustion	1.7 ± 0.2	0.50 ± 0.04
2%Er^{3+}, 1%Yb^{3+} Ball milling	122 ± 5	5.0 ± 0.2
2%Er^{3+}, 1%Yb^{3+} Combustion	80 ± 10	6.0 ± 0.5

Figure 5.17: Temporal evolution of Er^{3+} $^4S_{3/2}$ UC luminescence intensity in Y_2O_3: 2%Er^{3+}, 1%Yb^{3+} obtained by ball milling detecting at 17730 cm^{-1} upon excitation at 10256 cm^{-1}. The inset shows a detail of the intensity rise. The shadow region corresponds to the GSA/ESA contribution taking the intrinsic lifetime of the $^4S_{3/2}$ state after direct excitation.

the GSA/ESA and GSA/ETU contribution to the total intensity. Contributions of 99% and 1% have been estimated for GSA/ETU and GSA/ESA mechanisms, respectively [19].

The green ($^2H_{11/2}$, $^4S_{3/2}$) emission lifetimes for Y_2O_3: 2%Er^{3+}, 1%Yb^{3+} samples, observed upon excitation at 10256 cm^{-1}, are much longer than those obtained for samples doped with 20%Yb^{3+}. Even more, lifetimes after IR excitation are longer than lifetimes after direct Er^{3+} excitation at 20492 cm^{-1}. This highlights the energy transfer in which Yb^{3+} ions, with a longer lifetime of about 1000 μs, can feed the $^4I_{11/2}$ Er^{3+} multiplet after IR excitation. The same trend is observed for the red emission decay. The shorter lifetimes detected for samples doped with 20%Yb^{3+} are related to a back-transfer from Er^{3+} to Yb^{3+} ions whose probability increases with Yb^{3+} concentration (see Fig. 5.14).

Conclusions

Y_2O_3: Er^{3+}, Yb^{3+} nanocrystalline samples have been synthesized by two different methods, mechano-chemical synthesis and combustion reaction. A steady-state grain size of 25 nm is reached for the milled Y_2O_3 samples while average sizes of 10-15 nm are estimated for nanoparticles prepared by combustion. However, thermal treatments are required in order to reduce surface contamination responsible for the luminescence quenching and final sizes of ca. 50 nm are obtained for all samples. The nanocrystals have been protected in capillaries for optical studies and in some cases SiO_2-coated (10 nm thickness). In both cases, the optical properties are similar indicating the preservation of the nanocrystals for further surface contamination. The presence of a SiO_2 coating surface would allow to functionalize the nanoparticles for different applications. The dependence of optical properties on synthesis method or dopant concentration has been studied. The red to green intensity ratio can be tuned by changing Yb^{3+} concentration. More intense UC emission and longer lifetimes have been detected for ball milling samples making them more suitable for applications. GSA/ETU has been established to be the main mechanism responsible for the UC luminescence. An enhancement of red emission after IR excitation has been identified.

5.2.2 Er^{3+}, Yb^{3+} co-doped NaYF$_4$

Synthesis and characterization

Sodium yttrium fluoride, NaYF$_4$, can crystallize with two different phases, the hexagonal β-phase (space group $P-6$) and the cubic α-phase (space group $Fm3m$). As it will be discussed later, obtaining NaYF$_4$: Er^{3+}, Yb^{3+} nanoparticles in the pure β phase would be an important step to get a promising efficient UC material.

Figure 5.18 shows the XRD pattern of NaYF$_4$ nanoparticles co-doped with nominal concentrations of 2%Er^{3+}, 20%Yb^{3+}, synthesized in a planetary ball mill according to the reaction and the optimal parameters described in Section 3.2, and using different milling times. It must be noted that when milling time increases, both intensity and width of the peaks corresponding to the hexagonal phase increase and β-NaYF$_4$ is obtained for times longer than four hours. On the contrary, XRD peaks matching with cubic phase decrease when milling time increases. Peaks which do not coincide with any of these phases are related to the initial YF$_3$ and disappear for times longer than four hours.

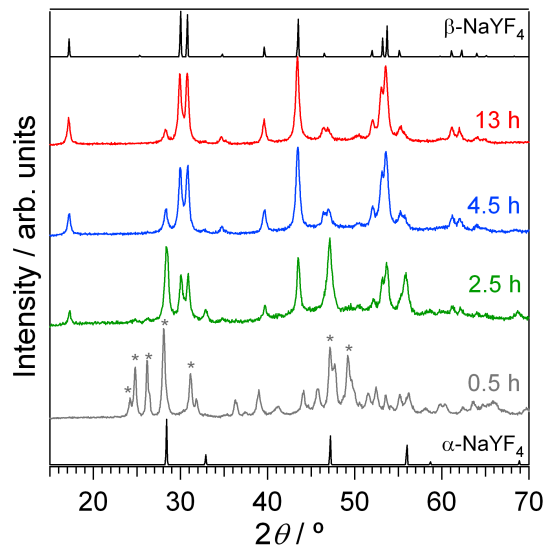Figure 5.18: XRD patterns of NaYF$_4$: 2%Er^{3+}, 20%Yb^{3+} for different milling times (0.5, 2.5, 4.5 and 13 hours). The calculated patterns for hexagonal β-NaYF$_4$ and cubic α-NaYF$_4$ are also shown. Asterisks indicate YF$_3$ peaks.

The average nanoparticles size is deduced from XRD peaks broadening according to the Williamson-Hall equation (eq. 4.1). The particle size estimated for NaYF$_4$: 2%Er^{3+}, 20%Yb^{3+} is about 33 nm after 4 hours milling (Fig. 5.19(a)), and 36 nm after 13 hours
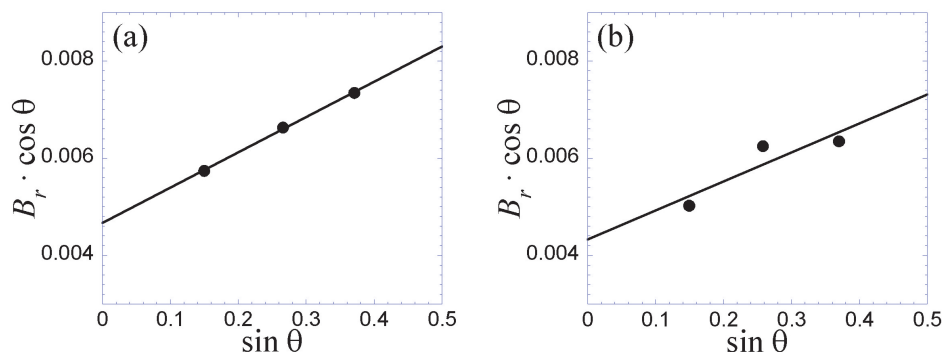
Figure 5.19: Particle size estimation for NaYF$_4$: 2%Er^{3+}, 20%Yb^{3+} nanoparticles prepared in the ball mill after 4.5 hours (a) and 13 hours (b) milling time. The fitting Williamson-Hall equations are given by $B_r \cos\theta = 0.00467 + 0.00727 \sin\theta$ (a) and $B_r \cos\theta = 0.00432 + 0.00599 \sin\theta$ (b) and the estimated sizes are L=33 nm (a) and L=36 nm (b), respectively.

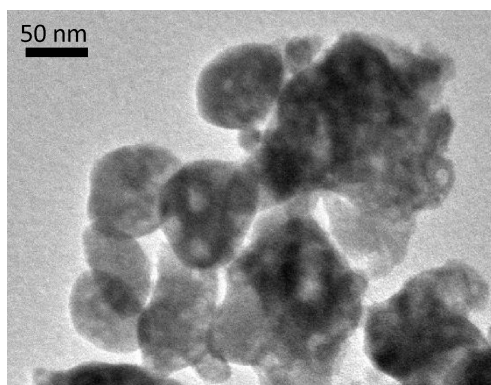Figure 5.20: TEM image of NaYF$_4$: 2%Er^{3+}, 20%Yb^{3+} nanocrystals prepared by ball milling.

(Fig. 5.19(b)). Therefore, it can be seen that from 4 hours, further milling time does not imply significant changes in particle size. Considering not only the hexagonal phase formation with the lower cubic contribution, but also the resultant nanocrystals size, it can be concluded that the optimum milling time for β-NaYF$_4$: 2%Er^{3+}, 20%Yb^{3+} is ca. 10 hours.

A TEM image of NaYF$_4$: 2%Er^{3+}, 20%Yb^{3+} nanocrystals prepared by ball milling after 13 hours grinding is shown in Fig. 5.20. An average size of ca. 50 nm is estimated, this value is slightly larger than the one obtained from XRD patterns broadening (36 nm). Particles are often aggregated forming bigger clusters.

In order to analyze the efficiency of these nanoparticles prepared by ball milling as UC phosphor material, their optical properties have been compared with the experimental
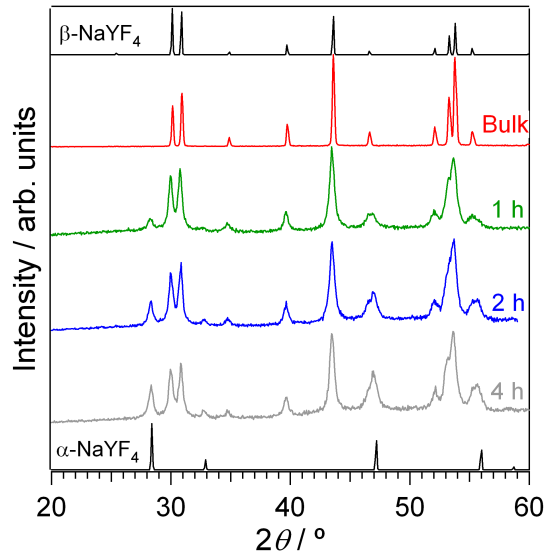
Figure 5.21: XRD patterns of NaYF$_4$: 2%Er^{3+}, 20%Yb^{3+} bulk and nanoparticles obtained for different grinding times (1, 2 and 4 hours). The calculated patterns for hexagonal β-NaYF$_4$ and cubic α-NaYF$_4$ are also shown.

results obtained for the bulk β-NaYF$_4$: 2%Er^{3+}, 20%Yb^{3+} synthesized by Krämer [2]. Moreover, NaYF$_4$: 2%Er^{3+}, 20%Yb^{3+} nanoparticles have also been obtained by milling this bulk β-NaYF$_4$ crystals of 2-5 μm in size in the planetary ball mill. This process has been carried out using ZrO$_2$ vials and balls, a ball to powder mass ratio of 20:1, an angular velocity of 300 rpm and stopping 5 minutes every 30 minutes of milling.

Figure 5.21 shows the XRD patterns of the as prepared NaYF$_4$: 2%Er^{3+}, 20%Yb^{3+} nanoparticles for 1, 2 and 4 hour milling and the bulk material. It is observed that the bulk crystallizes only in the hexagonal system, however, when grinding time increases, the hexagonal peaks intensity decreases while peaks corresponding to the cubic phase increase. From hexagonal peaks broadening an average size of 30 nm is obtained for both 1 and 4 hours milling time.

Optical properties

Hexagonal β-NaYF$_4$ doped with Er^{3+}-Yb^{3+} and Tm^{3+}-Yb^{3+} are up to now, the most efficient bulk materials for green and blue UC luminescence, respectively [2]. It is an order of magnitude more efficient than the cubic phase. This can be ascribed to the low vibrational energies in the hexagonal lattice, phonon cutoff around 350 cm^{-1}, which

reduces non-radiative multiphonon relaxation processes [20]. Besides, the high emission efficiency has also been attributed to the structural disorder of the lattice and the presence of multi-sites for Na^+ and RE^{3+} ions [21], [22]. Both the doping ratio and the phase purity determine the actual UC efficiency. $NaYF_4$: $2\%Er^{3+}$, $20\%Yb^{3+}$ colloidal nanocrystals showed a reduction in the UC efficiency by a factor of 10^2-10^3 [1]. Half of this diminution was believed to be due to the fact that the nanoparticles crystallize in the α phase, and the other half to the presence of OH^- impurities on the particles surface.

- **Synthesis method dependence.**

  In this work we compare optical properties and UC luminescence efficiency of $NaYF_4$: $2\%Er^{3+}$, $20\%Yb^{3+}$ β-bulk and nanoparticles prepared by milling the bulk hexagonal micropowders, and by the mechano-chemical reaction of the fluorides described in Section 3.2.
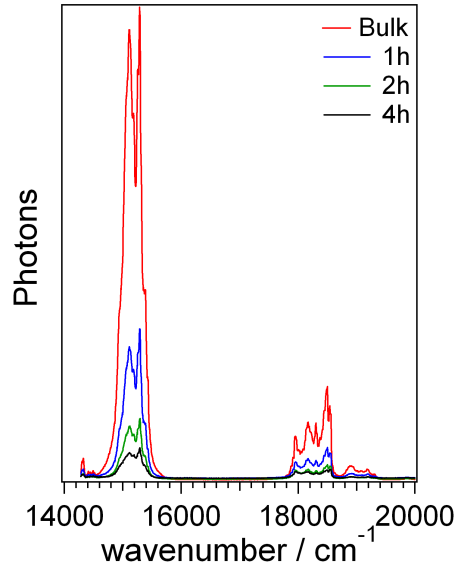

Figure 5.22: RT luminescence spectra of $NaYF_4$: $2\%Er^{3+}$, $20\%Yb^{3+}$ bulk and nanoparticles (30 nm) upon Er^{3+} excitation at 26596 cm^{-1}. Measurements were performed under the same experimental conditions.

  Figures 5.22 and 5.23 show the RT luminescence spectra of bulk β-$NaYF_4$: $2\%Er^{3+}$, $20\%Yb^{3+}$ and nanoparticles obtained by milling the bulk powders for 1, 2 and 4 hours (average size of 30 nm) upon direct Er^{3+} excitation at 26596 cm^{-1} and after IR excitation at 10256 cm^{-1}. Emission bands around 15000 and 18000 cm^{-1}

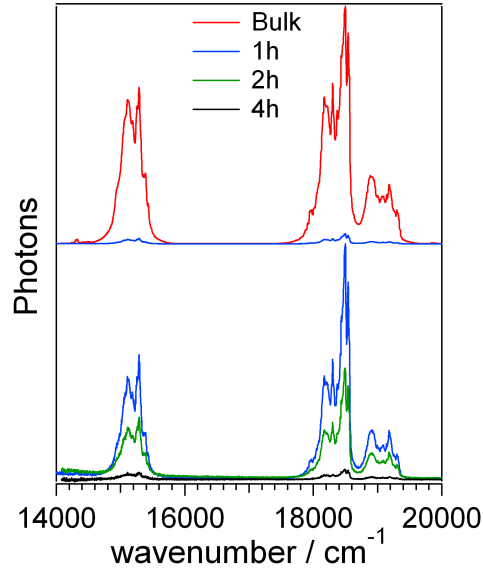Figure 5.23: RT UC emission spectra of NaYF$_4$: 2%Er^{3+}, 20%Yb^{3+} bulk and nanoparticles (30 nm) upon IR excitation at 10256 cm^{-1}. Measurements were carried out under the same experimental conditions.

detected in both cases are assigned to the red $^4F_{9/2} \rightarrow {}^4I_{15/2}$ and green ($^2H_{11/2}$, $^4S_{3/2}$) $\rightarrow {}^4I_{15/2}$ Er^{3+} transitions, respectively. It is worth mentioning that after visible excitation into the $^4G_{11/2}$ Er^{3+} level, red emission is more intense than green luminescence and when milling time increases from 1 to 4 hours, the red to green intensity ratio decreases by a factor of two. On the other hand, an enhancement of green emission upon IR excitation is detected for all samples. An evident reduction in the overall luminescence intensity is observed upon both visible and IR excitation for longer milling times. The intensity decrease is more noticeable in the UC luminescence and a reduction in the UC efficiency by a factor of 50 and 10^3 is estimated for NaYF$_4$: 2%Er^{3+}, 20%Yb^{3+} nanocrystals obtained after 1 and 4 hours milling, respectively. The low efficiency observed in nanoparticles is related to two different factors regarding the milling process. First, the cubic phase emergence which is less efficient than the hexagonal phase [2]. Second, the particles surface contamination with the vials and balls which is known to be one of the main problems in mechanical milling synthesis [23].

Figure 5.24 compares the RT UC luminescence spectra of NaYF$_4$: 2%Er^{3+}, 20%Yb^{3+} obtained using the two described procedures; by milling the hexagonal bulk doped
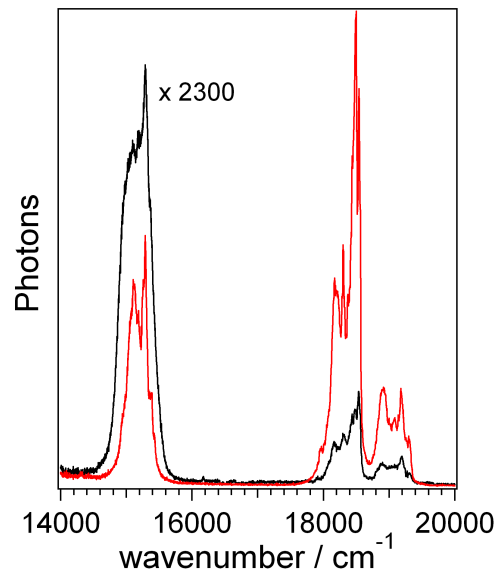
Figure 5.24: RT UC luminescence spectra of NaYF$_4$: 2%Er^{3+}, 20%Yb^{3+} prepared by milling the hexagonal bulk (red) and by the mechano-chemical reaction of the fluorides (black) upon IR excitation at 10256 $^{-1}$. Notice the scale factor.

NaYF$_4$ for 1 hour, and by the mechano-chemical reaction of the fluorides (NaF, YF$_3$, YbF$_3$, ErF$_3$) according to equation 3.2 for ten hours. In both cases, nanoparticles size is around 30-35 nm. It must be pointed out that the sample prepared from the fluorides reaction is much less efficient (notice the scale factor). The fact that in this sample the red emission is five times more intense than the green luminescence is also noteworthy. Since the impurity distribution during the mechano-chemical reaction is difficult to control, it might be very heterogenous. Therefore, there is a higher probability of finding nanoparticles with impurity concentration larger than nominal. This situation makes non-radiative process, responsible for the luminescence quenching, become more important in nanocrystals prepared by the mechano-chemical reaction.

- **Temporal evolution and UC mechanism.**

  The RT green $(^2H_{11/2}, {}^4S_{3/2}) \rightarrow {}^4I_{15/2}$ and red ${}^4F_{9/2} \rightarrow {}^4I_{15/2}$ Er^{3+} UC luminescence intensity versus the excitation power density at 10250 cm^{-1} for NaYF$_4$: 2%Er^{3+}, 20%Yb^{3+} nanoparticles obtained after 1 hour milling is plotted on a double logarithmic scale in Fig. 5.25. A quadratic power dependence is observed below 1 W·cm^{-2}
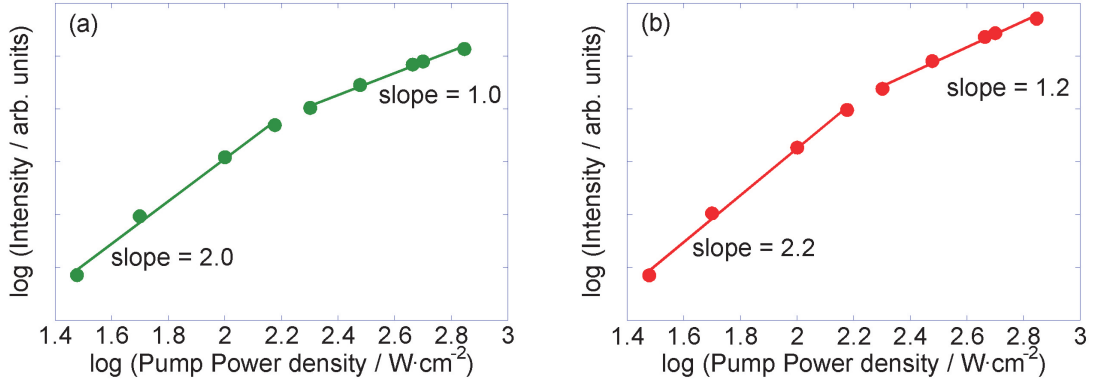
Figure 5.25: Excitation power dependence of the Er^{3+} green (a) and red (b) UC emission upon excitation at 10250 cm^{-1} for $NaYF_4$: $2\%Er^{3+}$, $20\%Yb^{3+}$ milled for 1 hour.

for both emissions, which is the typical behavior of a two-photon excitation process in the low-power regime. Hence, this behavior represents the experimental confirmation of a two-photon UC process. On the contrary, the slope decreases to 1.0 and 1.2 for green and red luminescence, respectively, at higher excitation power densities as explained by Pollnau *et al.* [24] and Suyver *et al.* [25].

RT temporal evolution of the red and green Er^{3+} UC luminescence in $NaYF_4$: $2\%Er^{3+}$, $20\%Yb^{3+}$ bulk and nanoparticles prepared by milling the bulk powders and by the mechano-chemical reaction of the fluorides have been measured upon visible and IR excitation (data not shown). The decays measured upon visible excitation at 20492 cm^{-1} have been fitted to a single exponential. In the experimental data obtained upon IR excitation at 10246 cm^{-1} a rise followed by a decay is detected, similarly to the case of Y_2O_3: Er^{3+}, Yb^{3+} nanoparticles described previously in this section. The UC emission decay have been fitted to a Vial's type equation [18]. The best fitting values are enclosed on tables 5.4 and 5.5, B and D being the decay and rise, respectively.

Comparing the temporal evolution of the luminescence intensity for $NaYF_4$: $2\%Er^{3+}$, $20\%Yb^{3+}$ bulk and nanoparticles, it can be seen that lifetimes obtained for bulk are systematically longer than those obtained for nanoparticles, for both red and green luminescence upon visible and IR excitation. This lifetime decrease associated to the size diminution is partially related to non-radiative process since, as we have

Table 5.4: Lifetimes of the $^4F_{9/2}$ Er^{3+} level in different NaYF$_4$: 2%Er^{3+}, 20%Yb^{3+} samples detecting at 15129 cm^{-1} after visible and IR excitation.

Sample	τ / μs (E_{exc}=20492 cm^{-1})	B / μs (E_{exc}=10246 cm^{-1})	D / μs (E_{exc}=10246 cm^{-1})
Bulk	385 ± 5	655 ± 5	60 ± 2
1 hour milled	145 ± 5	580 ± 10	230 ± 5
9.5 hours milled	54 ± 4	78 ± 5	5.8 ± 0.5

Table 5.5: Lifetimes of the $^4S_{3/2}$ Er^{3+} level in different NaYF$_4$: 2%Er^{3+}, 20%Yb^{3+} samples detecting at 18520 cm^{-1} after visible and IR excitation.

Sample	τ / μs (E_{exc}=20492 cm^{-1})	B / μs (E_{exc}=10246 cm^{-1})	D / μs (E_{exc}=10246 cm^{-1})
Bulk	116 ± 2	316 ± 5	42 ± 2
1 hour milled	33 ± 1	177 ± 6	60 ± 3
9.5 hours milled	11.5 ± 0.5	23.5 ± 0.8	2.3 ± 0.2

seen, it is accompanied by an intensity decrease. However, the intensity decrease is notably more important than the lifetime reduction. As an example, in NaYF$_4$: 2%Er^{3+}, 20%Yb^{3+} milled for 1 hour the green UC luminescence intensity diminishes by a factor of 50 while the lifetime is only reduced to half its value. This additional intensity reduction should be related to the cubic phase appearance.

Conclusions

NaYF$_4$: 2%Er^{3+}, 20%Yb^{3+} nanocrystals have been prepared by two different methods, and particles of around 30 nm in size are obtained in all cases. The sample obtained after milling the bulk for 1 hour shows the best UC luminescence efficiency but it is still much less efficient than bulk. This is related to the emergence of cubic α-NaYF$_4$, and to surface contamination of the nanocrystals during the milling process, associated to the larger surface-to-volume ratio in nanoparticles.

5.2.3 Tb^{3+} or Eu^{3+} and Yb^{3+} co-doped Gd$_3$Ga$_5$O$_{12}$ and Y$_3$Al$_5$O$_{12}$

Synthesis and characterization

Gadolinium gallium garnet, GGG, and yttrium aluminum garnet, YAG, are suitable materials as host for luminescent trivalent lanthanide ions. They belong to the cubic crystalline system, having a *garnet* structure, with $Ia3d$ space group (Fig. 5.26). The bulk cell parameters are a_0=12.376 Å and a_0=12.010 Å for GGG and YAG, respectively. For both systems, the *garnet* structure is composed of a 24(c) dodecahedral site (D_2 point symmetry) for Gd^{3+} or Y^{3+} depending on the case with a coordination number 8, and two sites for Ga^{3+} and Al^{3+}, respectively, a 16(a) octahedral site with a coordination number 6, and a 24(d) tetrahedral site of coordination number 4. O^{2-} ions occupy the 96(h) sites with each one being a member of two dodecahedra, one octahedron and one tetrahedron. The garnet structure can be viewed as interconnected dodecahedra, octahedra and tetrahedra with shared O atoms at the corners of the polyhedra. Taking into account the ionic radii, the doping RE^{3+} impurities are expected to enter into the Gd^{3+} or Y^{3+} sites which possess D_2 symmetry [26].
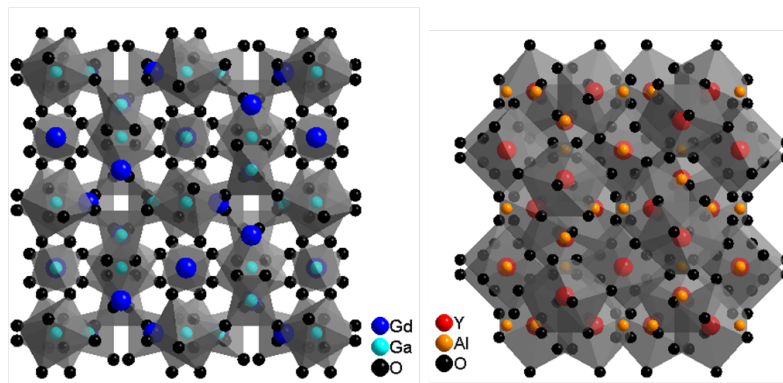

Figure 5.26: GGG (left) and YAG (right) cubic structures. In GGG structure the two Ga^{3+} sites with octahedral and tetrahedral coordination is shown, while the Y^{3+} site with coordination number 8 is depicted in YAG structure.

GGG and YAG nanocrystalline powders co-doped with nominal concentrations of 2%Tb^{3+}-5%Yb^{3+}, 2%Eu^{3+}-5%Yb^{3+}, and 2%Eu^{3+}-1%Er^{3+} have been prepared by the sol-gel Pechini's method described in Section 3.4. It is worth mentioning that lanthanides replace Gd^{3+} or Y^{3+} ions, hence, the amount of RE^{3+} doping ions (1%, 2% or 5% mol) is with respect to Gd^{3+} or Y^{3+}. All the prepared samples have been analyzed using the

XRD technique.

Figure 5.27 shows the XRD pattern of GGG: $2\%Eu^{3+}$, $5\%Yb^{3+}$. The Rietveld refinement of the GGG nanopowders XRD pattern is consistent with a cubic *garnet* single phase (space group $Ia3d$, $a=12.391$ Å) but contains small traces (up to 5%) of a second phase, Gd_3GaO_6. The obtained lattice constant is similar to that found for an Eu^{3+} doped GGG nanocrystalline sample prepared by the same Pechini procedure [27]. From Rietveld refinement and considering XRD peaks broadening, the average size of the crystallite grains has been determined to be ca. 30 nm. The Eu^{3+}-Er^{3+} doped GGG samples are also cubic *garnet* single phase apart from a small trace contamination of Gd_3GaO_6 phase, as found for the Eu^{3+}-Yb^{3+} doped samples.
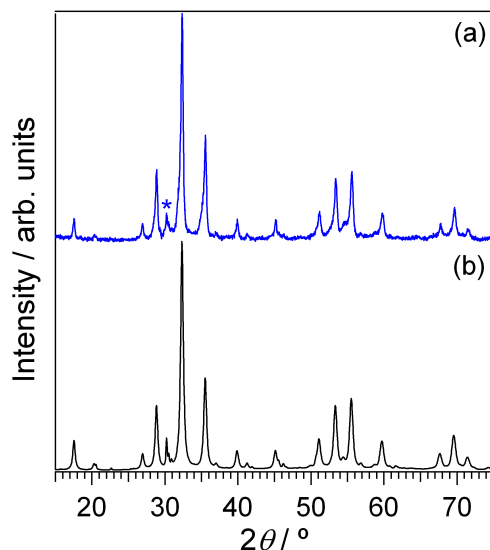

Figure 5.27: XRD pattern of GGG: $2\%Eu^{3+}$, $5\%Yb^{3+}$ prepared following Pechini's method (a) and Rietveld fit (b). The asterisk indicates the main peak of the Gd_3GaO_6 impurity phase.

Figure 5.28 presents the XRD pattern of YAG: $2\%Eu^{3+}$, $5\%Yb^{3+}$ together with the Rietveld fit. Both the Eu^{3+}-Yb^{3+} and Eu^{3+}-Er^{3+} doped nanocrystalline YAG samples crystallize only in the cubic *garnet* phase (space group $Ia3d$, $a=12.031$ Å) without evidence of contamination from other phases. The corresponding size of the nanoparticles obtained from Rietveld fitting is around 40 nm. There is no evidence of extra peaks due to phase segregation of the doping components.

TEM images of GGG and YAG nanocrystalline samples (see Fig. 5.29) show that the samples are made of particles of different shapes and sizes. Most of them are spherical

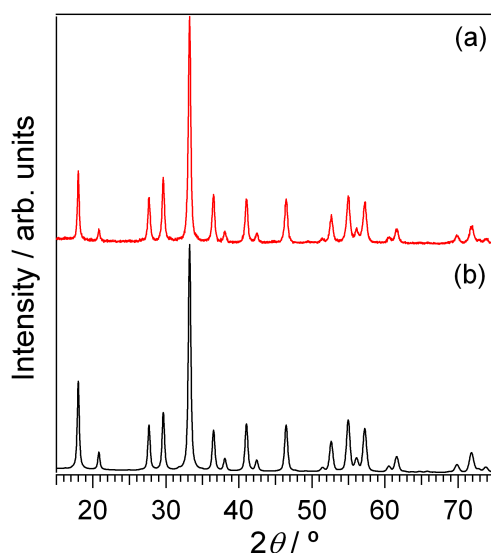with sizes in the 30-50 nm range but in some cases particles are aggregated forming larger clusters.

Figure 5.28: XRD pattern of YAG: 2%Eu^{3+}, 5%Yb^{3+} prepared by the sol-gel Pechini's method (a) and Rietveld fit (b).
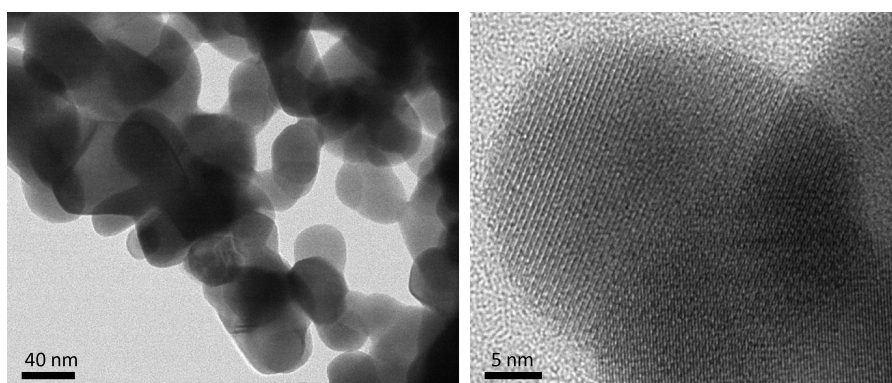

Figure 5.29: TEM images of GGG: 2%Tb^{3+}, 5%Yb^{3+} prepared by the sol-gel Pechini's method. In the HRTEM image, the observed interplanar distances (0.30 nm) corresponds to the (012) crystal plane.

Figure 5.30 shows IR absorption spectra of both host materials, GGG and YAG, between 300 and 1300 cm^{-1}. Analyzing this frequency range, information about vibrational energy of each matrix can be obtained. The higher energy absorption band is observed at around 680 cm^{-1} for the GGG, while it is shifted to higher energies and appears at around 800 cm^{-1} in YAG. The highest energy phonons belong to the Ga-O and Gd-O
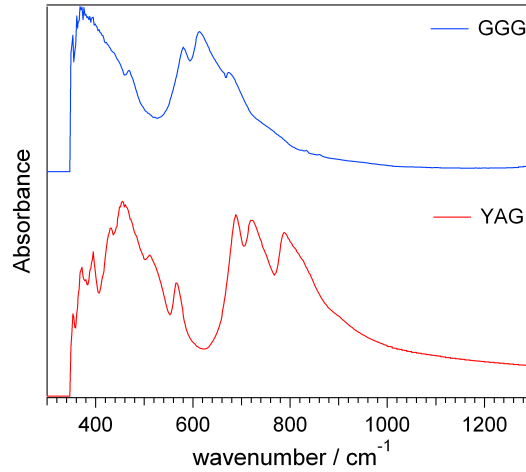
Figure 5.30: IR absorption spectra of GGG: $2\%Eu^{3+}$, $5\%Yb^{3+}$ and YAG: $2\%Eu^{3+}$, $5\%Yb^{3+}$ synthesized by Pechini's method. Nanopowders were diluted in KBr to perform these measurements.

or Y-O and Al-O stretching vibration modes for GGG and YAG, respectively [28]. According to the gap's law, multiphonon relaxation becomes much more probable for higher phonon energies. Therefore, non-radiative processes, responsible for the diminishing of luminescence, are more likely to happen in YAG than in GGG.

Optical properties

GGG and YAG are host materials with interesting optical properties [29]. Average phonon energy in sesquioxides is quite low for oxide materials, which is especially beneficial for optical applications. YAG: Nd^{3+} is one of the most important materials used for solid-state lasers. GGG has also shown to have several advantages over other laser materials [30]. A detailed investigation on the spectroscopy and excited state dynamics at RT has been carried out on Tb^{3+}-Yb^{3+} and Eu^{3+}-Yb^{3+} co-doped GGG and YAG.

- **Tb^{3+}-Yb^{3+} System.**

  Figure 5.31 shows Tb^{3+} excitation spectra in both GGG and YAG co-doped with $2\%Tb^{3+}$, $5\%Yb^{3+}$ nanoparticles. In addition to the f−f Tb^{3+} transitions from the ground state $^7F_6$ to different excited states plotted in the *Dieke diagram*, the excitation spectrum of YAG: $2\%Tb^{3+}$, $5\%Yb^{3+}$ shows two intense bands at around 31060 and 36100 cm^{-1}. We assign these transitions to the spin-allowed and spin-forbidden 4f−5d$_t$ transitions of Tb^{3+}, in agreement with the data reported by Dorenbos for
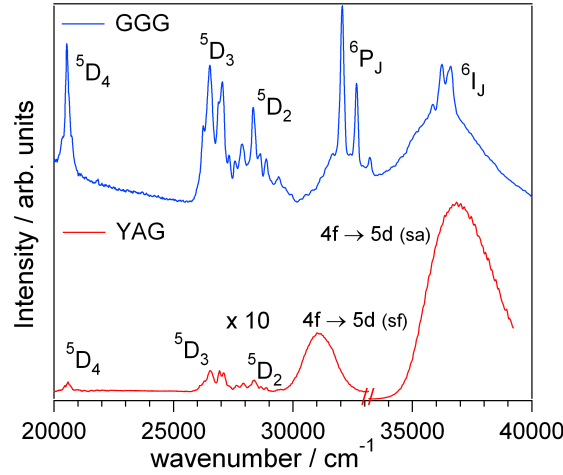
Figure 5.31: RT excitation spectra of GGG: $2\%\text{Tb}^{3+}$, $5\%\text{Yb}^{3+}$ and YAG: $2\%\text{Tb}^{3+}$, $5\%\text{Yb}^{3+}$ recording Tb^{3+} luminescence at 18420 cm^{-1}.

the same compound (36500 and 30860 cm^{-1}) [31], [32]. The high energy band is more than one order of magnitude stronger than the low energy band. Surprisingly, these bands are not detected in the case of GGG: $2\%\text{Tb}^{3+}$, $5\%\text{Yb}^{3+}$ pointing out a different crystal-field strength on the Tb^{3+} site.

Figure 5.32 presents Tb^{3+} $^5D_4 \rightarrow {}^7F_J$ emission upon UV excitation in the $5d_t$ state at 37040 cm^{-1} for GGG: $2\%\text{Tb}^{3+}$, $5\%\text{Yb}^{3+}$ and YAG: $2\%\text{Tb}^{3+}$, $5\%\text{Yb}^{3+}$ nanocrystalline samples. As expected from excitation spectra, Tb^{3+} luminescence is one order of magnitude more intense in YAG than in GGG.

Figure 5.33 compares the RT luminescence spectra of nanocrystalline GGG: $2\%\text{Tb}^{3+}$, $5\%\text{Yb}^{3+}$ and YAG: $2\%\text{Tb}^{3+}$, $5\%\text{Yb}^{3+}$ upon visible and IR excitation. The first is obtained exciting directly the Tb^{3+} ions at 37040 cm^{-1} while the UC luminescence is observed after the excitation of Yb^{3+} ions at 10250 cm^{-1}. In all cases, the emission bands observed in the red-blue region (15000-21000 cm^{-1}) are assigned to the transitions from the $^5D_4$ multiplet to lower energy ^7F_J states of Tb^{3+} ions (see Fig. 5.34). Yb^{3+} pairs luminescence is not detected in our samples.

The presence of the parity allowed $4f-5d_t$ transitions in the near-UV region in the case of YAG: $2\%\text{Tb}^{3+}$, $5\%\text{Yb}^{3+}$, and additionally, the demonstration of Tb^{3+}-Yb^{3+} UC luminescence, opens the possibility to use this system also as a downconversion
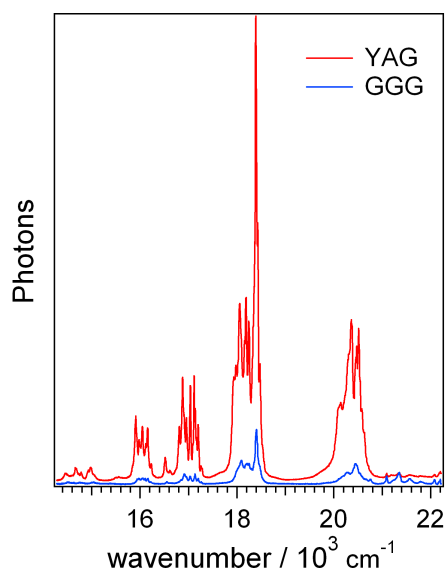
Figure 5.32: RT luminescence spectra of GGG: 2%Tb^{3+}, 5%Yb^{3+} and YAG: 2%Tb^{3+}, 5%Yb^{3+} upon excitation at 37040 cm^{-1}. Measurements were carried out under the same experimental conditions.
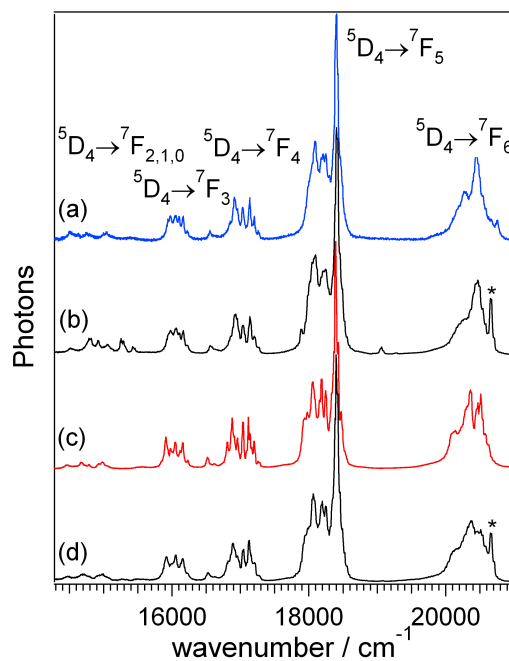

Figure 5.33: RT luminescence spectra of GGG: 2%Tb^{3+}, 5%Yb^{3+} exciting at 37040 cm^{-1} (a) and 10250 cm^{-1} (b). RT emission spectra of YAG: 2%Tb^{3+}, 5%Yb^{3+} exciting at 37040 cm^{-1} (c) and 10250 cm^{-1} (d). * is an artifact and represents the laser at twice the excitation frequency.
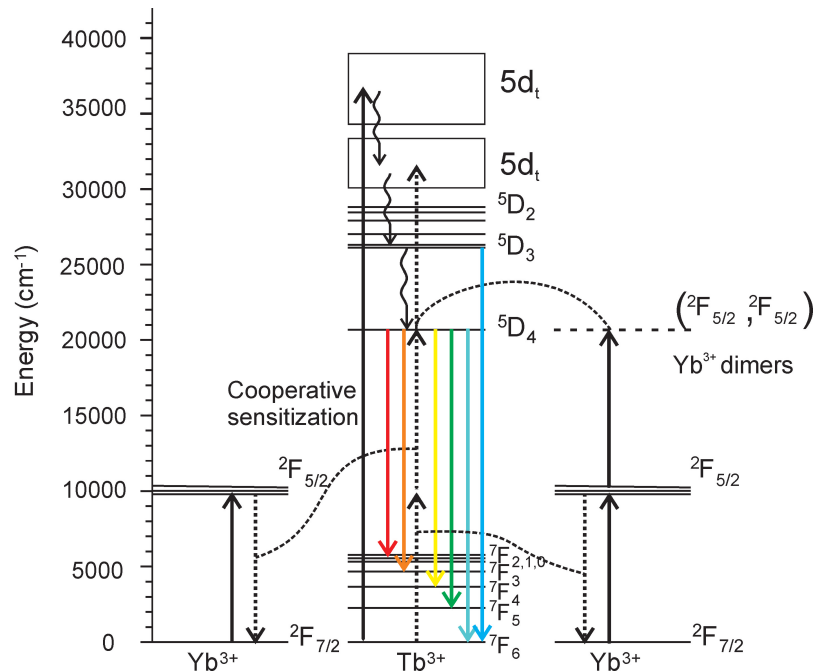
Figure 5.34: Energy level scheme of Tb^{3+} and Yb^{3+} ions with the $^5D_4 \rightarrow ^7F_J$ and the $^5D_3 \rightarrow ^7F_J$ Tb^{3+} luminescent transitions and the cooperative sensitization mechanism.

phosphor. In this process, one Tb^{3+} ion would generate two Yb^{3+} ions in the excited state [33]. This could be applied for the improvement of solar cells efficiency. This is particularly important taking into account that the $4f-5d_t$ bands in YAG: 2%Tb^{3+}, 5%Yb^{3+} are located close to band gap of clear glasses usually integrated in front of the solar cell panels as protectors.

As we have seen, the excitation spectrum of Tb^{3+} in YAG (Fig. 5.35(a)) consists of two strong bands, at 36100 cm^{-1} and 31060 cm^{-1}, compared to the intensity of the f$-$f transitions. Excitation on the $4f-5d_t$ bands is followed by a fast non-radiative relaxation to the $^5D_3$ and $^5D_4$ excited states, from where emission takes place (Fig. 5.35(b)). Although green $^5D_4 \rightarrow ^7F_J$ Tb^{3+} UC luminescence has been widely investigated, there are only few examples of blue Tb^{3+} UC emission from the $^5D_3$ multiplet in the literature [34], [35]. Luminescence from this state between 22000 and 27000 cm^{-1} has been observed after IR excitation of YAG: 2%Tb^{3+}, 5%Yb^{3+} (Fig. 5.35(c)).

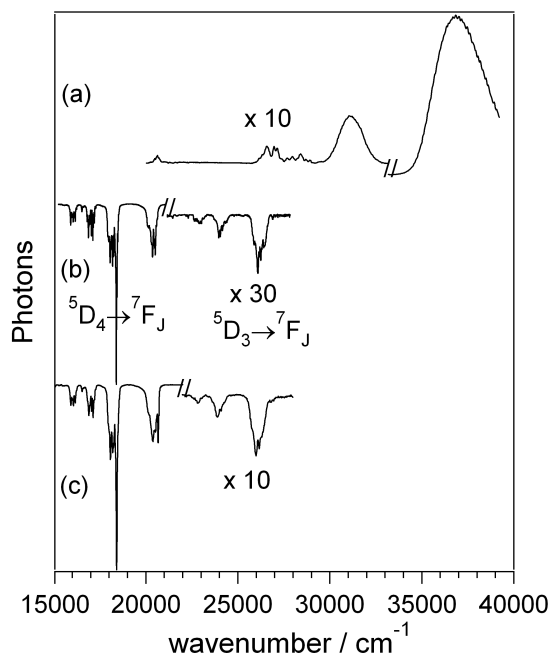The only way to access the $^5D_3$ excited state is via a three photon process (see

Figure 5.35: RT excitation spectrum of YAG: 2%Tb^{3+}, 5%Yb^{3+} (a), RT luminescence spectrum after excitation at 37037 cm^{-1} (b), and RT emission spectrum after excitation at 10250 cm^{-1} (c). Note the scale factors.

Fig. 5.34). In order to prove this assumption, the power dependence of the emitted photons of the $^5D_4 \rightarrow {}^7F_J$ and $^5D_3 \rightarrow {}^7F_J$ Tb^{3+} transitions upon IR excitation has been measured (Fig. 5.36). Slopes of 2.6 and 3.3 are obtained for $^5D_4 \rightarrow {}^7F_J$ and $^5D_3 \rightarrow {}^7F_J$ Tb^{3+} emissions, respectively. With this result, we can propose that a three photon process is also involved in the green $^5D_4 \rightarrow {}^7F_J$ luminescence, indicating the relevance of a non-radiative relaxation from the $^5D_3$ to $^5D_4$ states. Such a three photon process for the green UC Tb^{3+} emission was previously observed [36]. This is in agreement with a possible CR process populating the $^5D_4$ from the $^5D_3$ state [37].

- **Eu^{3+}-Yb^{3+} System.**

  Figure 5.37 presents Eu^{3+} luminescence upon excitation at 25450 cm^{-1} for GGG: 2%Eu^{3+}, 5%Yb^{3+} and YAG: 2%Eu^{3+}, 5%Yb^{3+} nanoparticles under the same experimental conditions. It can be observed that emission intensity is of the same order of magnitude for both cases. Emission features are different for Eu^{3+}-Yb^{3+} co-doped GGG and YAG nanoparticles. $^5D_0 \rightarrow {}^7F_{6,5}$ Eu^{3+} emission peaks are shifted to
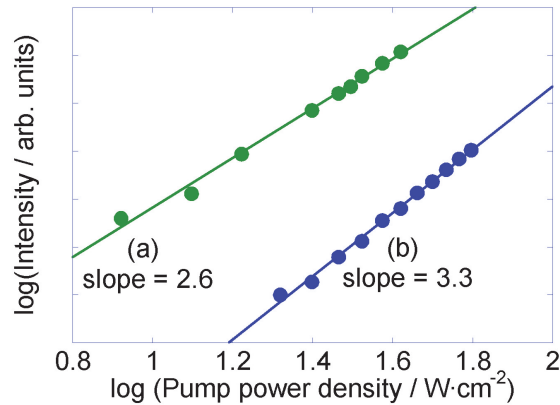
Figure 5.36: Excitation power dependence of the Tb^{3+} $^5D_4 \to$ ^7F_J luminescence (a) and Tb^{3+} $^5D_3 \to$ ^7F_J emission (b) in YAG: $2\%Tb^{3+}$, $5\%Yb^{3+}$ upon 10250 cm^{-1} excitation.

higher energies for GGG, $^5D_0 \to$ $^7F_{3,2}$ transitions have very diverse shape in GGG and YAG, and $^5D_0 \to$ $^7F_1$ transitions show different energy separation between lines.

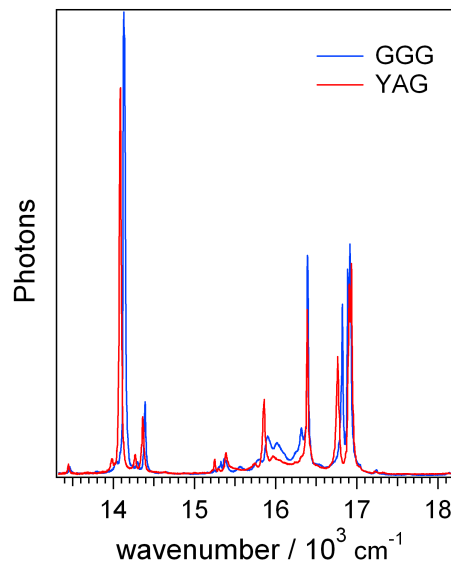Figure 5.37: RT emission spectra of GGG: $2\%Eu^{3+}$, $5\%Yb^{3+}$ and YAG: $2\%Eu^{3+}$, $5\%Yb^{3+}$ upon excitation at 25450 cm^{-1}. Measurements were carried out under the same experimental conditions.

Figure 5.38 shows the Stokes and anti-Stokes RT luminescence spectra of nanocrystalline GGG: $2\%Eu^{3+}$, $5\%Yb^{3+}$ and YAG: $2\%Eu^{3+}$, $5\%Yb^{3+}$. Eu^{3+} emission is obtained upon direct excitation at 25450 cm^{-1}, whereas Eu^{3+} UC luminescence is detected upon Yb^{3+} ions excitation at 10250 cm^{-1}. Unlike Yb^{3+} to Tb^{3+} UC luminescence, there are only few examples of Yb^{3+} to Eu^{3+} UC emission in the literature [13], [14], [38]. The bands observed in the spectra are assigned to $^5D_0 \to$

$^{7}F_{J}$ Eu^{3+} transitions (see Fig. 5.39). In the UC luminescence spectra (Fig. 5.38(b) and 5.38(d)), emission bands in the 14500-15500 cm^{-1} range due to Er^{3+} impurities are detected in addition to the Eu^{3+} f$-$f transitions. This fact was also observed by Tanner [38] even with starting materials with purity of 99.999%. In order to understand if Er^{3+} impurities play any role in the Yb^{3+} to Eu^{3+} UC luminescence process, GGG: 2%Eu^{3+}, 1%Er^{3+} and YAG: 2%Eu^{3+}, 1%Er^{3+} nanocrystalline samples have also been investigated.
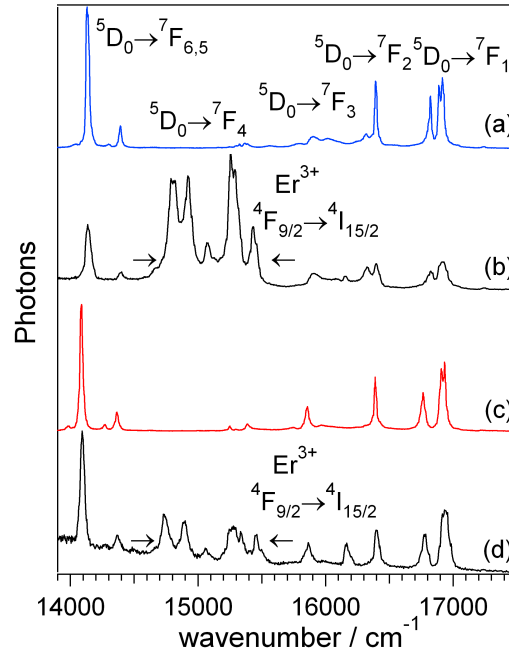

Figure 5.38: RT luminescence spectra of GGG: 2%Eu^{3+}, 5%Yb^{3+} exciting at 25450 cm^{-1} (a) and 10250 cm^{-1} (b). RT emission spectra of YAG: 2%Eu^{3+}, 5%Yb^{3+} exciting at 25450 cm^{-1} (c) and 10250 cm^{-1} (d). The emission corresponding to Er^{3+} transitions are shown between arrows.

Figure 5.40 compares the UC luminescence of GGG: 2%Eu^{3+}, 1%Er^{3+} upon excitation of Er^{3+} ions with a LD at 10250 cm^{-1} with that of GGG: 2%Eu^{3+}, 5%Yb^{3+}. Er^{3+} excitation at 10250 cm^{-1} (Fig. 5.40 (a)) is able to induce UC luminescence bands observed at around 15000 and 18000 cm^{-1}, assigned to the $^{4}F_{9/2} \rightarrow {}^{4}I_{15/2}$, and $(^{2}H_{11/2}, {}^{4}S_{3/2}) \rightarrow {}^{4}I_{15/2}$ Er^{3+} transitions, respectively, with the absence of Eu^{3+} emission. It is concluded that excitation at 10250 cm^{-1} induces Er^{3+} luminescence but it is not able to induce Eu^{3+} luminescence.

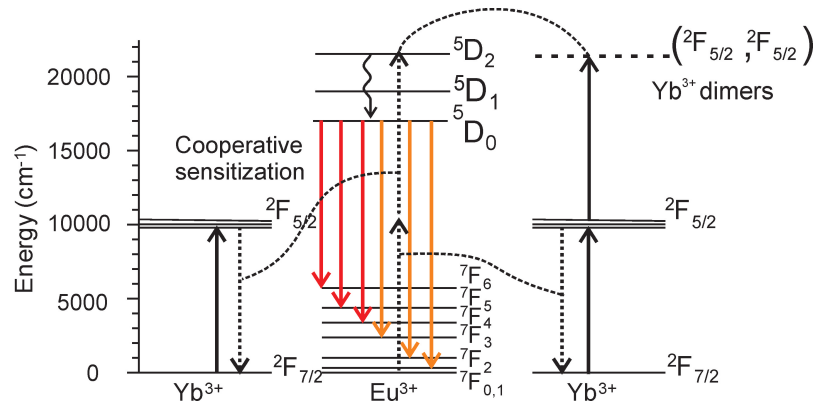Figure 5.39: Energy level diagram of Eu^{3+} and Yb^{3+} ions with the $^5D_0 \to^7 F_J$ Eu^{3+} emissions and the proposed Yb^{3+}-Eu^{3+} energy transfer mechanisms.
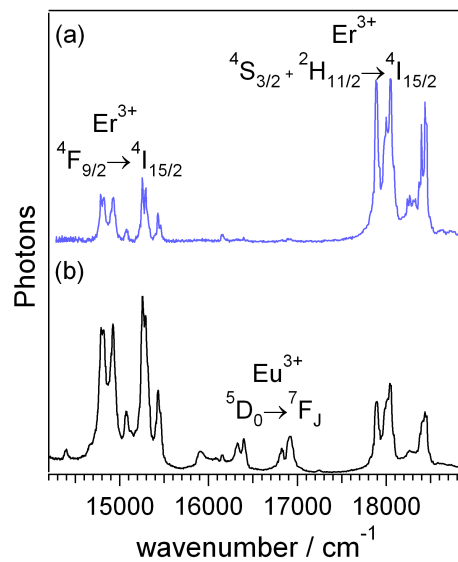

Figure 5.40: RT UC luminescence spectra of GGG: 2%Eu^{3+}, 1%Er^{3+} (a) and GGG: 2%Eu^{3+}, 5%Yb^{3+} (b) exciting at 10250 cm^{-1}.

Therefore, any relevant role of Er^{3+} in the Yb^{3+} to Eu^{3+} UC luminescence is excluded, although the efficient Yb^{3+} to Er^{3+} energy transfer compared to Yb^{3+} to Eu^{3+} one is pointed out.

- **Temporal evolution and UC mechanism.**

The time evolution of the $^5D_4 \to^7 F_J$ Tb^{3+} and $^5D_0 \to^7 F_J$ Eu^{3+} emission in GGG and YAG singly-doped and co-doped nanoparticles has been recorded after direct excitation at around 20365 and 16920 cm^{-1} for Tb^{3+} and Eu^{3+}, respectively. GGG experimental decays are shown in Fig. 5.41.

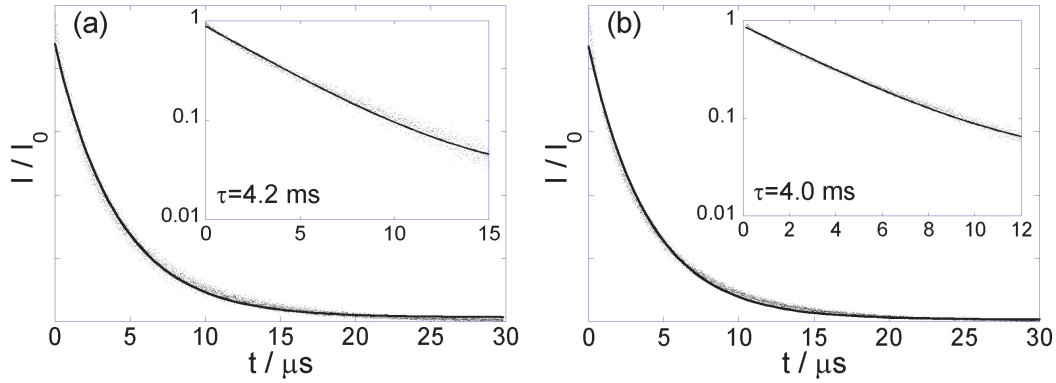Figure 5.41: Temporal evolution of $^5D_4 \rightarrow ^7F_J$ Tb^{3+} RT luminescence in GGG: 2%Tb^{3+}, 5%Yb^{3+} upon excitation at 20365 cm^{-1} (a), and $^5D_0 \rightarrow ^7F_J$ Eu^{3+} RT emission in GGG: 2%Eu^{3+}, 5%Yb^{3+} upon excitation at 16920 cm^{-1} (b).

Table 5.6: Lifetimes of the $^5D_4$ Tb^{3+} and $^5D_0$ Eu^{3+} levels in GGG and YAG samples measured at the emission energy, E$_{em}$, after direct excitation into the emitting levels.

E_{em}/cm^{-1}	Sample	τ/ms	Sample	τ/ms
18396	GGG: 2%Tb^{3+}, 5%Yb^{3+}	4.2 ± 0.2	GGG: 2%Tb^{3+}	4.1 ± 0.2
18396	YAG: 2%Tb^{3+}, 5%Yb^{3+}	4.9 ± 0.2	YAG: 2%Tb^{3+}	4.7 ± 0.2
14134	GGG: 2%Eu^{3+}, 5%Yb^{3+}	4.0 ± 0.2	GGG: 2%Eu^{3+}	4.1 ± 0.2
14090	YAG: 2%Eu^{3+}, 5%Yb^{3+}	4.6 ± 0.2	YAG: 2%Eu^{3+}	4.6 ± 0.2

Experimental data have been fitted to a single exponential for all samples and the corresponding lifetimes are shown in Table 5.6.

The Tb^{3+} and Eu^{3+} lifetimes obtained in this work are longer than the average values measured in doped Y$_3$GaO$_6$ [39] or Li$_2$SiO$_3$ [40] nanoparticles. It is also worth mentioning that the lifetimes for Tb^{3+} and Eu^{3+} ions in nanocrystalline GGG and YAG are significantly longer than the usual values found for the doped bulk oxide counterparts [41]. This behavior was also observed for nanocrystalline Eu^{3+} doped Y$_2$O$_3$ [42] and ZrO$_2$ [43] powders and it is compatible with the small particle size of the nanopowders, around 40 nm. In fact, this lengthening of the lifetimes can be ascribed to a lower refractive index (n$_{eff}$) surrounding the lanthanide ions in the nanocrystalline material, compared to the micrometer size host, according to a higher surface-to-volume ratio [42]. The lifetimes obtained by fitting the $^2F_{5/2}$ $\rightarrow$ $^2F_{7/2}$ Yb^{3+} luminescence decay to a single exponential in co-doped GGG and

Table 5.7: Lifetimes of the $^2F_{5/2}$ Yb^{3+} excited state in GGG and YAG samples measured detecting at 9750 cm^{-1} upon excitation at 10250 cm^{-1}.

Sample	τ/μs
GGG: 2%Tb^{3+}, 5%Yb^{3+}	595 ± 10
YAG: 2%Tb^{3+}, 5%Yb^{3+}	485 ± 10
GGG: 2%Eu^{3+}, 5%Yb^{3+}	555 ± 10
YAG: 2%Eu^{3+}, 5%Yb^{3+}	480 ± 10

YAG samples are shown in Table 5.7. The same lifetime values are observed for singly Tb^{3+} (or Eu^{3+}) doped samples and Tb^{3+}-Yb^{3+} (or Eu^{3+}-Yb^{3+}) co-doped ones. Hence, there is no evidence of back-transfer from Tb^{3+} or Eu^{3+} to Yb^{3+}.

Tb^{3+} and Eu^{3+} UC luminescence has been measured in GGG and YAG upon excitation at 10250 cm^{-1} in the $^2F_{5/2}$ Yb^{3+} level. Tb^{3+} and Eu^{3+} ions have no excited states resonant with the $^2F_{7/2} \rightarrow {}^2F_{5/2}$ Yb^{3+} transition in the IR region. Therefore, the UC emission cannot be explained by a direct transfer (GSA/ETU) from the excited Yb^{3+} to a Tb^{3+} or Eu^{3+} ion. A cooperative GSA/ESA mechanism in Tb^{3+}-Yb^{3+} dimers coupled by exchange was demonstrated to be responsible for Tb^{3+} UC emission after Yb^{3+} excitation in Cs$_3$Tb$_2$Br$_9$: Yb^{3+} at low temperatures [12]. However, GGG and YAG crystal structures are not able to accommodate Tb^{3+}-Yb^{3+} or Eu^{3+}-Yb^{3+} dimers. Hence, GSA/ESA in dimers can be ruled out as a mechanism responsible for the UC luminescence. Additionally, UC phenomena in YF$_3$: Tb^{3+}, Yb^{3+} were explained as a cooperative sensitization [10]. Strek *et al.* proposed two mechanisms to explain the anti-Stokes Eu^{3+} emission in KEu$_{0.2}$Yb$_{0.8}$(WO$_4$)$_2$ upon Yb^{3+} excitation, which were cooperative sensitization and a process based on Yb^{3+} pairs [13].

The unambiguous manner to investigate the mechanism involved in the UC luminescence is to study its temporal evolution under pulsed excitation [12]. The cooperative sensitization, a three ions process, involves energy transfer from two sensitizers (Yb^{3+} ions) to the activator (Tb^{3+} or Eu^{3+}). This is a slow process which is active during the Yb^{3+} lifetime. The temporal evolution of the $^5D_4 \rightarrow {}^7F_J$
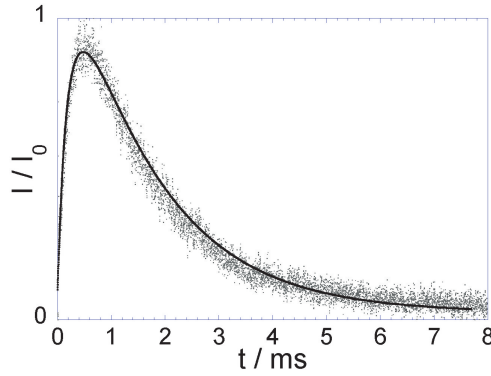
Figure 5.42: Temporal evolution of Tb^{3+} UC emission intensity in YAG: 2%Tb^{3+}, 5%Yb^{3+} detecting at 18396 cm^{-1} after pulsed excitation at 10250 cm^{-1}.

green UC luminescence of Tb^{3+} obtained upon Yb^{3+} excitation at 10250 cm^{-1} for the YAG: 2%Tb^{3+}, 5%Yb^{3+} sample is shown in Fig. 5.42. The rise of the emission intensity after IR excitation is a clear fingerprint of an energy transfer process. The cooperative sensitization is proposed as the mechanism responsible for Tb^{3+} UC luminescence in GGG and YAG systems co-doped with Yb^{3+}. This mechanism involves three ions and is depicted in Fig. 5.34. The cooperative sensitization responsible for the Tb^{3+} UC luminescence is as follows: two Yb^{3+} ions in the excited state transfer non-radiatively the energy to the $^5D_4$ states of Tb^{3+}. The same cooperative sensitization mechanism would be expected in the Eu^{3+}-Yb^{3+} UC luminescence (see Fig. 5.39). The Tb^{3+} lifetime observed in the UC decay transients, 1.8 ± 0.1 ms, is shorter than the one obtained after direct excitation, 4.9 ± 0.2 ms. (See Fig. 5.42 and Table 5.6). This difference is related to the fact that not all Tb^{3+} have necessarily an Yb^{3+} ion as a close neighbor. In UC measurements, only those Tb^{3+} which are close to Yb^{3+} ions are excited, whereas after direct excitation, all Tb^{3+} are involved in the luminescence [44].

The temporal evolution in Tb^{3+}-Yb^{3+} systems can be simulated by considering a cooperative sensitization mechanism. Taking into account the four level system schematically shown in Fig. 5.43, we can write down the four coupled differential rate equations (eq. 5.1) describing the populations of each level, N_i:
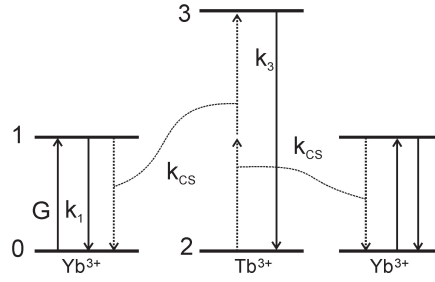
Figure 5.43: Diagram of the cooperative sensitization of Tb^{3+} UC luminescence. In this process two excited Yb^{3+} ions transfer non-radiatively their energy to Tb^{3+} ions.

$$
\begin{aligned}
\frac{dN_0}{dt} &= -GN_0 + \frac{N_1}{\tau_1} + 2k_{CS}N_1^2 N_2 \\
\frac{dN_1}{dt} &= GN_0 - \frac{N_1}{\tau_1} - 2k_{CS}N_1^2 N_2 \\
\frac{dN_2}{dt} &= \frac{N_3}{\tau_3} - k_{CS}N_1^2 N_2 \\
\frac{dN_3}{dt} &= -\frac{N_3}{\tau_3} + k_{CS}N_1^2 N_2
\end{aligned}
\qquad (5.1)
$$

where τ_1 and τ_3 represent the Yb^{3+} $^2F_{5/2}$ and Tb^{3+} $^5D_4$ experimental lifetimes, respectively, G is the power dependence GSA rate constant and k_{CS} is the cooperative sensitization rate parameter. The physical meaning of these equations is the following; the rise is related with half of the Yb^{3+} $^2F_{5/2}$ lifetime, that would correspond to the lifetime of Yb^{3+} pairs, whereas the decay is related to the Tb^{3+} $^5D_4$ lifetime. N_0 and N_2 are known from Yb^{3+} and Tb^{3+} concentration values, respectively, whereas N_1 and N_3 are an initial hypothesis since they cannot be experimentally measured in an accurate manner. Values of 485 ± 10 μs (see Table 5.7) and 1.8 ± 0.1 ms (see Fig. 5.42) have been obtained from independent measurements for τ_1 and τ_3, respectively, in YAG: $2\%Tb^{3+}$, $5\%Yb^{3+}$. It is possible to obtain the only unknown parameter, k_{CS}, by fitting the time dependent evolution of the UC luminescence, obtained experimentally after short-pulsed excitation into the Yb^{3+} $^2F_{5/2}$ level, to this set of equations (Fig. 5.42). In this way, a value of 1350 s^{-1} has been determined for the energy transfer rate constant, $k_{CS}N_1N_2$.